

THE STAR FORMATION LAW IN NEARBY GALAXIES ON SUB-KPC SCALES

F. BIGIEL¹, A. LEROY¹, F. WALTER¹, E. BRINKS², W. J. G. DE BLOK³, B. MADORE⁴, M. D. THORNLEY⁵

Accepted for Publication in The Astronomical Journal

ABSTRACT

We present a comprehensive analysis of the relationship between star formation rate surface density, Σ_{SFR} , and gas surface density, Σ_{gas} , at sub-kpc resolution in a sample of 18 nearby galaxies. We use high resolution HI data from THINGS, CO data from HERACLES and BIMA SONG, $24\mu\text{m}$ data from the *Spitzer* Space Telescope, and UV data from GALEX. We target 7 spiral galaxies and 11 late-type/dwarf galaxies and investigate how the star formation law differs between the H₂-dominated centers of spiral galaxies, their HI-dominated outskirts and the HI-rich late-type/dwarf galaxies. We find that a Schmidt-type power law with index $N = 1.0 \pm 0.2$ relates Σ_{SFR} and Σ_{H_2} across our sample of spiral galaxies, i.e., that H₂ forms stars at a constant efficiency in spirals. The average molecular gas depletion time is $\sim 2 \cdot 10^9$ years. The range of Σ_{H_2} over which we measure this relation is $\sim 3 - 50 M_{\odot} \text{pc}^{-2}$, significantly lower than in starburst environments. We find the same results when performing a pixel-by-pixel analysis, averaging in radial bins, or when varying the star formation tracer used. We interpret the linear relation and constant depletion time as evidence that stars are forming in GMCs with approximately uniform properties and that Σ_{H_2} may be more a measure of the filling fraction of giant molecular clouds than changing conditions in the molecular gas. The relationship between total gas surface density (Σ_{gas}) and Σ_{SFR} varies dramatically among and within spiral galaxies. Most galaxies show little or no correlation between Σ_{HI} and Σ_{SFR} . As a result, the star formation efficiency (SFE), $\Sigma_{\text{SFR}}/\Sigma_{\text{gas}}$, varies strongly across our sample and within individual galaxies. We show that this variation is systematic and consistent with the SFE being set by local environmental factors: in spirals the SFE is a clear function of radius, while the dwarf galaxies in our sample display SFEs similar to those found in the outer optical disks of the spirals. We attribute the similarity to common environments (low-density, low-metallicity, HI-dominated) and argue that shear (which is typically absent in dwarfs) cannot drive the SFE. In addition to a molecular Schmidt law, the other general feature of our sample is a sharp saturation of HI surface densities at $\Sigma_{\text{HI}} \approx 9 M_{\odot} \text{pc}^{-2}$ in both the spiral and dwarf galaxies. In the case of the spirals, we observe gas in excess of this limit to be molecular.

Subject headings: radio lines: galaxies — radio lines: ISM — galaxies: ISM — galaxies: evolution

1. INTRODUCTION

A robust, quantitative measurement of the relationship between star formation rate (SFR) and gas density (SF law) is of major astrophysical importance in the context of galaxy evolution: it describes how efficiently galaxies turn their gas into stars and constrains theoretical models of star formation; in addition, it serves as essential input to simulations and models of galaxy evolution (e.g., Springel & Hernquist 2003; Boissier & Prantzos 1999; Tan et al. 1999; Krumholz & McKee 2005; Matteucci et al. 2006). Direct observations of this relationship at sub-kpc scales are still very rare because measuring the distributions of star formation, atomic gas, and molecular gas at high resolution and sensitivity is challenging and time-consuming.

However, the past few years have seen an explosion in multiwavelength data for nearby galaxies. From

the ‘GALEX Nearby Galaxy Survey’ (Gil de Paz et al. 2007) and the ‘*Spitzer* Infrared Nearby Galaxies Survey’ (SINGS, Kennicutt et al. 2003) the distribution of star formation is now known in a large suite of local galaxies. From the ‘BIMA Survey of Nearby Galaxies’ (BIMA SONG, Helfer et al. 2003) and recent observations with the IRAM 30m telescope (HERACLES, Leroy et al. 2008b) the CO distributions of many nearby galaxies are also known. With ‘The HI Nearby Galaxy Survey’ (THINGS, Walter et al. 2008), HI maps that match or exceed the angular resolution and sensitivity of the ultraviolet, infrared, and CO data are now available for 34 nearby galaxies. In this paper, we combine this suite of multiwavelength data to measure the surface densities of HI, H₂, and SFR (Σ_{HI} , Σ_{H_2} , and Σ_{SFR}) across the entire optical disks of 18 nearby galaxies at 750 pc spatial resolution. Using these measurements, we examine the relationships among these three quantities across our sample.

Following the pioneering work of Schmidt (1959), it is common to relate gas density to the SFR density using a power law. He suggested the form $\rho_{\text{SFR}} \sim (\rho_{\text{gas}})^n$, where ρ_{SFR} and ρ_{gas} denote the volume densities of the SFR and the gas. Studying the distribution of HI and stars perpendicular to the Galactic plane, he derived a power-law index of $n \approx 2$. Sanduleak (1969) and Hartwick (1971)

¹ Max-Planck-Institut für Astronomie, Königstuhl 17, 69117, Heidelberg, Germany; bigiel@mpia.de

² Centre for Astrophysics Research, University of Hertfordshire, Hatfield AL10 9AB, U.K.

³ Department of Astronomy, University of Cape Town, Private Bag X3, Rondebosch 7701, South Africa

⁴ Observatories of the Carnegie Institution of Washington, Pasadena, CA 91101, USA

⁵ Department of Physics and Astronomy, Bucknell University, Lewisburg, PA 17837, USA

carried out the first measurements of the Schmidt law in other galaxies. They used bright stars in the Small Magellanic Cloud and H II regions in M31, respectively, to trace star formation and focused their analyses on *surface* densities, Σ_{HI} and Σ_{SFR} , which are directly observable (i.e., $\Sigma_{\text{SFR}} \sim (\Sigma_{\text{gas}})^N$). They found $N_{\text{SMC}} = 1.84 \pm 0.14$ and $N_{\text{M31}} = 3.50 \pm 0.12$. Throughout this paper, we use the term Schmidt law or star formation law (SF law) to refer to a power law formalism relating star formation surface density to atomic, molecular, or total gas surface density. Note that for a constant scale height, the exponents N and n are identical, i.e., it does not matter whether one considers volume or surface densities.

Madore et al. (1974) compared stars and H II-regions to Σ_{HI} and derived a higher power law index for the outer part than for the inner part of M33. Newton (1980) repeated this analysis with higher-resolution H I data and confirmed this behavior. Tosa & Hamajima (1975) compared H II-regions to Σ_{HI} in M31 and the LMC and find $N \approx 2$ for both galaxies. Hamajima & Tosa (1975) performed the same analysis in 7 nearby galaxies. They derived power law indices $N = 1.5 - 2.9$ and found radial variations in N for 2 of their sample galaxies (M31 and M101).

Kennicutt (1989, 1998a, hereafter K98) studied the globally averaged relationship between SFR and gas in a sample of 61 nearby normal spiral and 36 infrared-selected starburst galaxies. K98 showed that a Schmidt law relates the disk-averaged total gas surface density, $\Sigma_{\text{gas}} = \Sigma_{\text{HI}} + \Sigma_{\text{H}_2}$, to the disk-averaged star formation surface density, Σ_{SFR} , over many orders of magnitude. His subsample of normal spiral galaxies yields a power-law index $N = 2.47 \pm 0.39$; his composite sample, including starburst galaxies, yields $N = 1.40 \pm 0.15$. Similar studies of the disk-averaged Schmidt Law used a range of SFR tracers – such as H α , UV, radio continuum, and FIR emission – and found $N = 0.9 - 1.7$ (e.g., Buat et al. 1989; Buat 1992; Deharveng et al. 1994).

Other authors studied a local Schmidt law using radial profiles (i.e., comparing azimuthally averaged values) of Σ_{SFR} and Σ_{gas} . Wong & Blitz (2002) found $N = 1.2 - 2.1$ for 6 molecule-rich spiral galaxies. Boissier et al. (2003) derived $N \approx 2$ for 16 galaxies and Misiriotis et al. (2006) obtained $N = 2.18 \pm 0.20$ for the Milky Way. Heyer et al. (2004) found $N = 3.3 \pm 0.1$ for M33. For M51, Schuster et al. (2007) found $N = 1.4 \pm 0.6$ and Kennicutt et al. (2007), using 520 pc apertures centered on H α and 24 μm emission peaks, found $N = 1.56 \pm 0.04$.

The large range of power-law indices in the literature, $N \approx 1 - 3$, suggests that either different SF laws exist in different galaxies or that N is very sensitive to systematic differences in methodology (e.g., the choice of SFR tracers, the spatial resolution of the data, etc.). There are physically motivated, theoretical reasons to expect N in the range 0.75 – 2, and the precise value of N may vary with the regime one considers. Krumholz & McKee (2005) argue that a giant molecular cloud (GMC) will convert its gas into stars over a free-fall time, $t_{\text{ff}} \propto \rho_{\text{gas}}^{-0.5}$. If this is the case, then from the observation that the surface density of GMCs is constant (e.g., Solomon et al. 1987; Blitz et al. 2007), implying $\rho_{\text{gas}} \propto M_{\text{GMC}}^{-0.5}$, one expects $N \approx 0.75$ for the case where we measure the Schmidt law for individual GMCs. If we instead com-

pare uniform populations of GMCs, where the different molecular gas surface densities reflect only different *numbers* of clouds (not different physical properties), then one expects $N \approx 1$ for the molecular gas exponent (assuming the population-averaged timescale over which a GMC converts its gas into stars is constant). If gravitational instability in the neutral (H I+H₂) ISM is the key process in star formation, the SFR may instead depend on the free-fall time of the *total* gas; in this case, and if the gas scale height is constant, $t_{\text{ff}} \propto \Sigma_{\text{gas}}^{-0.5}$ and one would expect $N \approx 1.5$ (e.g., Madore 1977). Finally, if one postulates that star formation is a fundamentally collisional process, because, e.g., it may depend on the formation of H₂ by collisions between hydrogen atoms and dust grains or the collision of small clouds to form larger clouds, one would expect $\rho_{\text{SFR}} \propto \rho_{\text{gas}}^2$, which will lead to $N \approx 2$ (again for a system with constant gas scale height).

Another open question is whether the Schmidt law is fundamentally a molecular phenomenon or if a single, universal power law relates total gas and star formation. Because all stars are believed to form in molecular clouds, it would seem natural that H₂ and SFR are more immediately related than H I or total gas and SFR. Therefore it is somewhat surprising that observations remain contradictory on this point. One of the most surprising findings by K98 was that Σ_{SFR} correlated better with Σ_{HI} than with Σ_{H_2} in normal disks; the strongest correlation, between Σ_{SFR} and Σ_{gas} , was only marginally stronger than the $\Sigma_{\text{SFR}} - \Sigma_{\text{HI}}$ correlation. Wong & Blitz (2002) found a much stronger relationship between Σ_{SFR} and Σ_{H_2} than between Σ_{SFR} and Σ_{HI} , even finding an anti-correlation between Σ_{SFR} and Σ_{HI} at high SFRs, but they focused on molecule-rich spirals and therefore did not include large amounts of the H I-dominated ISM. Even in H₂-rich spirals, the question is still open. Recently, Schuster et al. (2007) and Crosthwaite & Turner (2007) studied the molecular gas-rich spirals NGC 5194 and NGC 6946 and found that the total gas correlates better with the SFR than H₂ alone.

This paper attempts to answer the following questions: how do the SFR, H₂, and H I surface densities relate to one another in nearby galaxies on a pixel-by-pixel basis? Which of these relationships are common across our sample, and which vary with environment? To address these questions, we measure Σ_{HI} , Σ_{H_2} , and Σ_{SFR} in a sample of 18 galaxies: 7 spirals which have central areas (hereafter loosely referred to as centers) dominated by molecular gas (‘spirals’) and 11 H I-dominated galaxies. We look at how these relationships differ between the H₂-dominated centers of the spirals, their H I-dominated outskirts, and H I-rich late type galaxies. By probing out to the optical radius r_{25} , i.e., where the B-band magnitude drops below 25 mag arcsec⁻², and including late-type galaxies, we are able to strongly constrain the universality of the various Schmidt laws.

We organize this analysis as follows: we describe the datasets used to measure Σ_{HI} , Σ_{H_2} , and Σ_{SFR} in §2. We explain how we convert these data to physical units and how we generate a set of independent measurements over the disk of each galaxy. In §3 we show the observed relationships between Σ_{HI} , Σ_{H_2} , and Σ_{SFR} for individual galaxies. We carry out power law fits to each distribution and assess whether there is a common Schmidt law

shared by all of our galaxies. We show results for spirals and H I-dominated late-type galaxies separately to highlight the range of environments in our sample. In §4 we combine our data for the spirals and for the H I-dominated galaxies, to be able to draw general conclusions about H I, H₂, and the SFR in these two samples. In §5 we explore the effect of environment by comparing the Schmidt law in the inner, H₂-dominated parts of spirals to their H I-dominated outer disks and to H I-dominated dwarf and late-type galaxies. We show that the relationship between total gas and SFR is a clear function of environment and fit the radial dependence of the molecular-to-atomic gas ratio in spirals. In §6 we summarize our results and give our conclusions. Here we also compare our results to those from previous studies.

2. SAMPLE, DATA, UNITS, AND MEASUREMENTS

This work is made possible by the existence of the state-of-the-art multiwavelength data sets mentioned in the introduction. We use high resolution H I data from ‘The H I Nearby Galaxy Survey’ (THINGS, Walter et al. 2008) and CO maps from a large ongoing project using HERA on the IRAM 30m telescope (HERACLES, Leroy et al. 2008b) and from the BIMA SONG survey (BIMA SONG, Helfer et al. 2003). We trace star formation combining mid-IR maps from the ‘*Spitzer* Infrared Nearby Galaxies Survey’ (SINGS, Kennicutt et al. 2003) and FUV maps from the ‘GALEX Nearby Galaxy Survey’ (NGS, Gil de Paz et al. 2007). In this section we describe our sample and these datasets, show maps and radial distributions, and explain how we generate measurements of Σ_{HI} , Σ_{H_2} , and Σ_{SFR} .

2.1. Sample

Our sample of spiral galaxies consists of the cross-section of THINGS, SINGS, the GALEX NGS and the HERACLES or BIMA-SONG CO surveys. Galaxies that are known to be H I-dominated are not required to be part of HERACLES or BIMA-SONG. This ensures that we measure at least the dominant component of the neutral ISM and the SFR along most lines of sight. Table 1 lists our sample along with their adopted properties: distance, inclination, position angle, radius (Walter et al. 2008, except that we adopt $i = 20^\circ$ in M51) and morphology (from LEDA, Prugniel & Heraudeau 1998). We separate the galaxies into two groups: 7 large spiral galaxies that have an H₂-dominated ISM in their centers (‘spirals’) and 11 late-type galaxies that are H I-dominated throughout.

We do not study galaxies with inclinations $> 70^\circ$ that would otherwise qualify for the sample. High inclinations yield very few sampling points and result in a deprojected beam elongated parallel to the minor axis in the plane of the galaxy, making it difficult to carry out fits to the data and interpret the results. We also do not include any galaxies more distant than 12 Mpc. This is the maximum distance at which the typical angular resolution of our data corresponds to our common spatial resolution of 750 pc.

We work without CO maps for 4 late-type spirals, NGC 925, NGC 2403, NGC 2976, NGC 4214 and 7 dwarf irregular galaxies. For most of these galaxies, the CO content is either measured or constrained by a significant upper limit: major axis profiles by Young et al.

TABLE 1
SAMPLE PROPERTIES¹

Galaxy	D [Mpc]	i [deg]	PA [deg]	r_{25} [arcmin]	Hubble type
H I-dominated Galaxies					
DDO 154	4.3	66	230	0.97	Irr
DDO 53	3.6	31	132	0.39	Irr
Ho I	3.8	12	50	1.66	Irr
Ho II	3.4	41	177	3.30	Irr
IC 2574	4.0	53	56	6.44	SABm
M81 DwA	3.6	23	49	0.63	Irr
M81 DwB	5.3	44	321	0.56	Irr
NGC 925	9.2	66	287	5.36	Scd
NGC 2403	3.2	63	124	7.92	SABc
NGC 2976	3.6	65	335	3.62	Sc
NGC 4214	2.9	44	65	3.38	Irr
Spirals With H ₂ -Dominated Centers					
NGC 628	7.3	7	20	4.89	Sc
NGC 3184	11.1	16	179	3.71	SABc
NGC 3521	10.7	73	340	4.16	SABb
NGC 4736	4.7	41	296	3.88	Sab
NGC 5055	10.1	59	102	5.87	Sbc
NGC 5194	8.0	20	172	3.88	Sbc
NGC 6946	5.9	33	243	5.74	SABc

¹ See Walter et al. (2008) for further information on individual galaxies and for references to the values quoted in this table.

(1995) for NGC 925, NGC 2403, and NGC 2976 (which is also part of BIMA SONG); Kitt Peak 12m mapping of the inner disk of NGC 2403 (Thornley & Wilson 1995); OVRO mapping of NGC 4214 by Walter et al. (2001); single dish pointings toward NGC 4214, Holmberg I and DDO 154 by Taylor et al. (1998); central pointings for DDO 53, IC 2574, and Holmberg II by Leroy et al. (2005). In each case, the ISM is well-established to be H I-dominated. M81 DwA and M81 DwB, two extremely low-mass dwarf irregular companions to M81, both lack CO measurements, but should also be H I-dominated. Of these galaxies, 8 have absolute B -band magnitudes fainter than -18 mag and maximum rotation velocities $\lesssim 100$ km s⁻¹ (i.e., they have the mass of the LMC or less). NGC 925 and NGC 2403 have $M_B \sim -20$ mag and maximum rotational velocities ~ 100 km s⁻¹; they are probably intermediate in mass between the LMC and M 33.

2.2. Data

2.2.1. THINGS H I Maps

To estimate the surface density of neutral atomic hydrogen, Σ_{HI} , we use VLA maps of the 21 cm line obtained as part of ‘The H I Nearby Galaxy Survey’ (THINGS, Walter et al. 2008). THINGS consists of high-resolution, high-sensitivity H I data for 34 nearby galaxies obtained with the NRAO⁶ VLA. The target galaxies have distances of $2 \leq D \leq 15$ Mpc and cover a wide range in star formation rates, H I masses, luminosities and Hubble Types.

The FWHM of the primary beam (field-of-view) is $32'$. We use ‘robust’ weighted maps, which have a typical beam size of $\sim 6''$. The typical 1σ RMS noise at our working resolution of 750 pc (see §2.3) is $\sigma(\Sigma_{\text{HI}}) \approx 0.5 M_\odot \text{pc}^{-2}$. Because our analysis is restricted to the

⁶ The National Radio Astronomy Observatory is a facility of the National Science Foundation operated under cooperative agreement by Associated Universities, Inc.

regime within the optical radius r_{25} (see §2.4 and compare the radial profiles in §2.5), the measured H I surface densities are safely above this sensitivity limit for all galaxies.

The integrated H I intensity map for NGC 6946 at our working resolution of 750 pc is shown as an example in the left panel of Figure 1. Further details regarding the data products and data reduction are given in Walter et al. (2008).

2.2.2. HERACLES CO Maps

We derive Σ_{H_2} distributions from two sources: an ongoing nearby galaxy survey using the HERA focal plane array on the IRAM 30m telescope (HERACLES, Leroy et al. 2008b), and the ‘BIMA Survey of Nearby Galaxies’ (BIMA SONG, Helfer et al. 2003). The profiles from the two sets of CO maps agree with one another and also with the major axis pointings from the FCRAO survey (Young et al. 1995). We use the HERACLES maps where available because they have good extent and sensitivity, often measuring CO well into the H I-dominated regime where (on average) $\Sigma_{\text{HI}} > \Sigma_{\text{H}_2}$, i.e., beyond the H₂-to-H I transition radius. Extending beyond the transition radius is critical to be able to differentiate between a molecular and total gas Schmidt law.

We use HERACLES maps for 6 spiral galaxies: NGC 628, NGC 3184, NGC 3521, NGC 4736, NGC 5055 and NGC 6946. These were obtained at the IRAM 30m telescope during January and October 2007 and further details are described in Leroy et al. (2008b). We show the CO intensity map for NGC 6946 in the middle panel of Figure 1. HERA maps the CO $J = 2 \rightarrow 1$ transition with an angular resolution of $11''$. For technical details on HERA see Schuster et al. (2004). Our maps are sensitive to surface densities $\Sigma_{\text{H}_2} \approx 3 \text{ M}_{\odot} \text{ pc}^{-2}$.

BIMA SONG produced maps of CO $J = 1 \rightarrow 0$ emission with good resolution, $\sim 7''$, but limited field of view. We use these maps only for NGC 5194. Also, we use these data to compare CO to the SFR at high resolution in the central parts of all 7 centrally H₂-dominated galaxies. The BIMA SONG map for NGC 5194 used here includes zero-spacing data from the Kitt Peak 12m telescope, making it sensitive to extended structure. The BIMA SONG maps we use are sensitive to surface densities above $\Sigma_{\text{H}_2} \approx 10 \text{ M}_{\odot} \text{ pc}^{-2}$.

2.2.3. GALEX FUV Data

We use FUV data from the ‘GALEX Nearby Galaxy Survey’ (NGS, Gil de Paz et al. 2007) to estimate Σ_{SFR} (see §2.3.2). The GALEX observatory provides simultaneous imaging in a far UV (FUV) and a near UV (NUV) broadband filter. The FUV band covers the wavelength range 1350–1750 Å, the NUV covers 1750–2800 Å. The angular resolutions (FWHM) are $4.0''$ and $5.6''$ for the FUV and the NUV respectively, and the field-of-view of the instrument is 1.25° . For technical details on the detector see Morrissey et al. (2005).

We remove a single set of foreground stars from the GALEX and *Spitzer* 24 μm maps (see §2.2.4). Foreground stars are prominent in the NUV images but much less so in the FUV images, and we find that we can identify them easily via their UV colors. We therefore use the NUV maps to identify foreground star candidates

and apply an NUV/FUV ratio cut of $NUV/FUV > 10$. We apply this to all emission above 5σ in the NUV maps, below this we cannot distinguish stars from noise. In a few cases, a cut-off higher than 10 was necessary to remove particularly bright foreground stars. We estimate the contribution from foreground stars below 5σ in our FUV images beyond $2r_{25}$ (where there is only marginal emission from our target galaxies) and find that their contribution is negligible.

We estimate and remove a small background from the FUV maps. We measure this away from the galaxy by discarding emission with intensities $> 3\sigma$ above the median value of the image. The background adopted is the median of this residual map and is subsequently subtracted from the original map. The backgrounds in the GALEX maps are very well behaved and this simple subtraction yields good results in most cases. For three galaxies – NGC 4214, NGC 5194 (M51), and NGC 6946 – we blank portions of the map that show the edge of the GALEX field-of-view, obvious artifacts, bright stars not entirely removed by the color-cut as well as M51b. These are usually located well away from the galaxy and have minimal impact on this study (which is restricted to the optical disks of the galaxies).

We correct the FUV maps for the effects of Galactic extinction. We estimate $E(B - V)$ from the extinction maps of Schlegel, Finkbeiner & Davis (1998) and convert to FUV extinction using $A_{\text{FUV}} = 8.24 \times E(B - V)$ (Wyder et al. 2007).

2.2.4. Spitzer Space Telescope 24 μm Data

FUV data are heavily affected by internal extinction. To estimate the amount of star formation obscured by dust (see §2.3.2), we use 24 μm data obtained by the ‘*Spitzer* Infrared Nearby Galaxies Survey’ (SINGS, Kennicutt et al. 2003). The map of NGC 4214 comes from the public archive. These data are scan maps taken with the MIPS instrument on board the *Spitzer* Space Telescope (Rieke et al. 2004). Full details of the observing strategy and target sensitivity are described by Kennicutt et al. (2003). The MIPS data were processed using the MIPS Instrument Team Data Analysis Tool (Gordon et al. 2005).

The SINGS observations were designed to detect emission out to the optical radius and in most of our targets this goal was achieved. The FWHM of the MIPS PSF at 24 μm is $6''$, though the beam is substantially non-Gaussian outside the central peak. This is only a minor concern for this study because to achieve a common spatial resolution for all data, we work with a typical angular resolution of $\sim 20''$.

We perform the following additional processing on the SINGS maps: we first blank the edges of the scan maps parallel to the direction of the scan; in these regions the noise increases and artifacts are more common. We also blank the stars identified from the GALEX images. We then subtract a background, which is usually quite small, using the same procedure as for the GALEX images. In a few maps – Ho I, NGC 3521 and NGC 6946 – we identify regions with unreliable background and blank these by hand. These regions are far away from the galaxy though and so have minimal effect on this analysis.

2.3. Alignment, Units, and Convolution

From the data described above, we construct maps of star formation rate surface density, Σ_{SFR} , atomic hydrogen surface density, Σ_{HI} , molecular hydrogen surface density, Σ_{H_2} , and total gas surface density, Σ_{gas} .

We place all of these maps on the THINGS astrometric grid (pixel scale: $1.5''$) at a common spatial resolution of 750 pc. We carry out most of our work at 750 pc resolution but also create versions of each map at a range of spatial resolutions, from the native resolution to 10 kpc (in steps of 50 pc below 1 kpc, and 500 pc up to 10 kpc). When degrading the resolution of a map, we convolve with a circular Gaussian beam (on the sky), i.e., we do not account for the inclination of the galaxy. For a given spatial resolution, this exercise may be thought of as moving each galaxy at a larger distance.

2.3.1. Gas Surface Density Maps

The total gas surface density, Σ_{gas} , is the sum of the atomic gas surface density, Σ_{HI} , and the molecular gas surface density, Σ_{H_2} (we do not consider ionized gas, as this makes up only a small fraction of the total gas content). Where Σ_{H_2} is below the sensitivity limit (see § 2.2.2), we take $\Sigma_{\text{gas}} = \Sigma_{\text{HI}}$, which is formally a lower limit. These quantities all have units of $M_{\odot} \text{ pc}^{-2}$ and are *hydrogen* surface densities, i.e., they do not include any contribution from helium. To scale our quoted surface densities to account for helium, one should multiply them by a factor of ~ 1.36 . All surface and column densities quoted in this paper have been corrected for the inclinations given in Table 1.

We assume a ratio $I(2 \rightarrow 1)/I(1 \rightarrow 0) = 0.8$, a typical number derived from comparing our maps to the maps of Helfer et al. (2003), Young et al. (1995) and Kuno et al. (2007). A detailed comparison between these datasets can be found in Leroy et al. (2008b). To convert from Σ_{CO} to Σ_{H_2} , we adopt a CO-to- H_2 conversion factor of $2.0 \times 10^{20} \text{ cm}^{-2} (\text{K km s}^{-1})^{-1}$. This value is appropriate for the Milky Way according to γ -ray and FIR studies (e.g., Strong & Mattox 1996; Dame et al. 2001), but slightly lower than the conversion factor suggested by virial mass methods (e.g., Solomon et al. 1987; Blitz et al. 2007). We do not account for any changes in the conversion factor with metallicity or other environmental factors. For comparison, we note that we use the same conversion factor adopted by Wong & Blitz (2002) but that K98 adopted a higher value of $2.8 \times 10^{20} \text{ cm}^{-2} (\text{K km s}^{-1})^{-1}$.

2.3.2. Star Formation Rate Surface Density Maps

We measure star formation rate surface densities, Σ_{SFR} , in units of $M_{\odot} \text{ yr}^{-1} \text{ kpc}^{-2}$, by combining FUV and $24\mu\text{m}$ maps. The GALEX FUV images trace predominantly O and early B stars and therefore offer a picture of recent, unobscured star formation. FUV emission can be heavily affected by dust, however, making it difficult to derive unbiased measurements of Σ_{SFR} from the FUV alone. Fortunately, the dust that obscures the FUV emission from young stars is heated and reradiates in the mid-infrared. The $24\mu\text{m}$ maps thus allow us to estimate the amount of ongoing dust-obscured star formation.

This approach was proposed and validated for individual star forming regions and large portions of galactic disks by Calzetti et al. (2007) and Kennicutt et al.

(2007). They showed that $24\mu\text{m}$ emission could be used to accurately estimate the amount of extinction that affects $\text{H}\alpha$ emission. We adopt an analogous approach and combine FUV and $24\mu\text{m}$ using the following formula:

$$\Sigma_{\text{SFR}} [M_{\odot} \text{ yr}^{-1} \text{ kpc}^{-2}] = 3.2 \times 10^{-3} I_{24} [\text{MJy ster}^{-1}] \quad (1) \\ + 8.1 \times 10^{-2} I_{\text{FUV}} [\text{MJy ster}^{-1}],$$

where Σ_{SFR} denotes the star formation rate surface density, and I_{24} and I_{FUV} are the $24\mu\text{m}$ and FUV intensities respectively. Leroy et al. (2008a) motivate the choice of coefficients in Equation 1. Σ_{SFR} derived from Equation 1 agrees with the values derived using the $\text{H}\alpha + 24\mu\text{m}$ calibration from Calzetti et al. (2007) at 750 pc resolution; when $I_{24} = 0$, Equation 1 reduces to the FUV-SFR calibration by Salim et al. (2007). SFRs integrated over entire galaxies as well as values derived from azimuthally averaged radial profiles agree well with those based on extinction-corrected $\text{H}\alpha$ emission alone.

As an example we show the Σ_{SFR} map for NGC 6946, which was derived using Equation 1, in the right panel of Figure 1. The RMS noise varies from map to map, but a typical limit for the sensitivity of the SFR maps is $\approx 1 \times 10^{-4} M_{\odot} \text{ yr}^{-1} \text{ kpc}^{-2}$. For our calibration of Σ_{SFR} we adopt the IMF from Calzetti et al. (2007), which is the default IMF in STARBURST99 (Leitherer et al. 1999), i.e., a Kroupa-type two-component IMF that extends to $120 M_{\odot}$. To convert to the truncated Salpeter (1955) IMF adopted by, e.g., Kennicutt (1989, 1998a) or Kennicutt et al. (2007), one should multiply our Σ_{SFR} by a factor of 1.59.

Because this particular combination of FUV and mid-IR maps is new, we compare our results to those obtained using maps of $\text{H}\alpha$ and $\text{H}\alpha + 24\mu\text{m}$ emission wherever these are available. For this purpose, we use $\text{H}\alpha$ maps from the SINGS Data Release 4. We fit and remove backgrounds from these maps, masking out any region with a particularly problematic background. We correct for [NII] in the bandpass following Calzetti et al. (2007) and for Galactic extinction using the dust maps of Schlegel, Finkbeiner & Davis (1998). We use $\text{H}\alpha$ maps for all of our spiral galaxies except NGC 4736.

In addition to sampling our data on a pixel-by-pixel basis at 750 pc resolution, we also show the results of our analysis carried out in azimuthally-averaged radial profiles and explore the effects of degrading to lower resolution (so that each ‘pixel’ contains many square kpc). Further, we compare our results to measurements from other studies using a variety of SF tracers (see § 6.2). These tests are shown in the appropriate sections below and lead us to conclude that our SFR maps are accurately tracing the amount and distribution of recent star formation.

2.4. Individual Data Points

With maps of Σ_{HI} , Σ_{H_2} , and Σ_{SFR} in hand, the next step is to generate individual data points. We compare these quantities over the entire optical disk of each galaxy, out to $r_{25} = d_{25}/2$. This is a departure from previous studies, which used integrated measurements over entire galaxy disks (e.g., Kennicutt 1989, 1998a), radial profiles (e.g., Wong & Blitz 2002), or apertures centered on $\text{H}\alpha$ and $24\mu\text{m}$ emission peaks (e.g., Kennicutt et al.

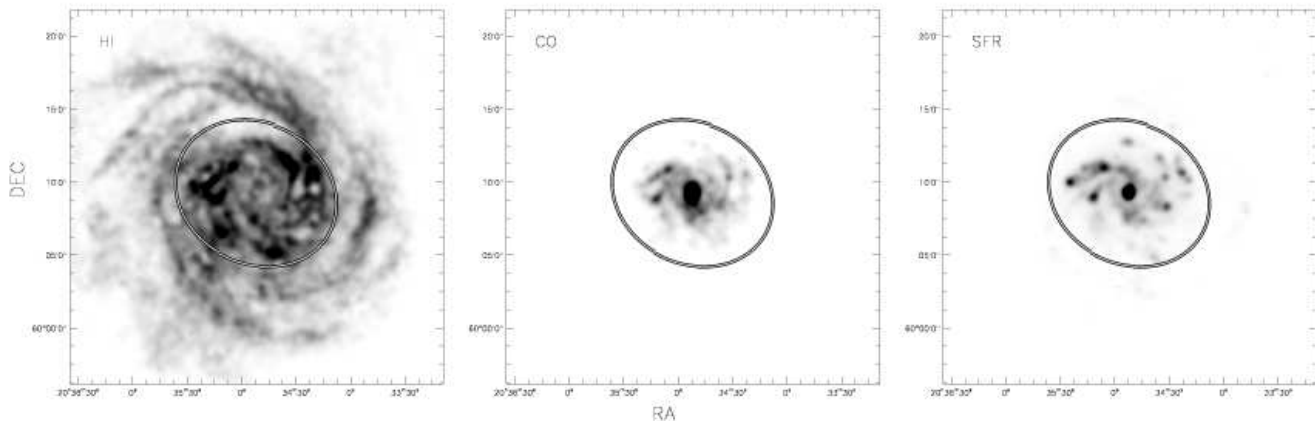


FIG. 1.— Maps of integrated H I (left), CO (middle) and SFR (right) surface densities at our working resolution of 750 pc for the spiral galaxy NGC 6946. The ellipses indicate the optical radius (r_{25}) in the plane of the galaxy, within which we compare Σ_{HI} , Σ_{H_2} , and Σ_{SFR} . Almost all star formation occurs within this radius, although the H I often extends much beyond r_{25} . The maps for all other galaxies in our study are shown in Leroy et al. (2008a).

2007).

We choose r_{25} as an outer limit. Most star formation takes place within this radius (e.g., see the profiles of Martin & Kennicutt 2001; Wong & Blitz 2002) and our FUV, $24\mu\text{m}$, and H I maps detect emission at more than 3σ over most of this area. The ellipses in Figure 1 show the projected optical radius, i.e., the extent of the region that we study, on the THINGS H I, HERACLES CO and Σ_{SFR} maps for NGC 6946. We refer the reader to Leroy et al. (2008a) for a ‘galaxy atlas’ showing all Σ_{HI} , Σ_{H_2} , and Σ_{SFR} maps for the galaxies in our sample.

We draw independent data points from our maps so that each data point corresponds to non-overlapping resolution elements and the data together cover the optical disk. This may be thought of as either reducing the oversampled map (rebinning the map) so that one pixel corresponds to a resolution element or as covering the disk with non-overlapping apertures equal in size to a resolution element. For each independent data point we measure Σ_{HI} , Σ_{H_2} , $\Sigma_{\text{gas}} = \Sigma_{\text{HI}} + \Sigma_{\text{H}_2}$, and Σ_{SFR} .

When convolving the maps with progressively larger beams (see § 2.3), flux from outside our radius cut at r_{25} would be convolved into the optical disk. To avoid this, the radius cut we use is decreased by half a beam width and is actually $r_{\text{max}} = r_{25} - 0.5\theta_{\text{beam}}$, where θ_{beam} is the FWHM of the beam in the same units as the radius. Note that θ_{beam} is subtracted in the plane of the sky, not the plane of the galaxy because the convolution takes place in the plane of the sky.

2.5. Radial Profiles

We also extract from our maps radial profiles of Σ_{HI} , Σ_{H_2} , and Σ_{SFR} and examine them along with the pixel-by-pixel data. We show the profiles for the spirals and 8 of our H I-dominated galaxies in Figures 2 and 3. We note that the radial profiles as well as the H I, CO and SFR maps for all of our galaxies are shown in Leroy et al. (2008b). The plots in Figures 2 and 3 show Σ_{SFR} , Σ_{HI} and Σ_{H_2} as a function of galactocentric radius normalized by r_{25} . The top axis gives the radius in kpc. Each point represents the average value in an individual $10''$ -wide tilted ring within 60° of the major axis using the struc-

ture parameters given in Table 1. For the H I-dominated galaxies, we show only Σ_{SFR} and Σ_{HI} .

3. THE STAR FORMATION LAW IN INDIVIDUAL GALAXIES

Figure 4 shows the relationship between gas and star formation surface densities in individual spiral galaxies. Color contours show the results from pixel-by-pixel sampling the optical disks of the 7 spiral galaxies in our sample. Each row shows results for a different galaxy. The columns left to right show Σ_{SFR} on the y-axis as a function of Σ_{HI} (left), Σ_{H_2} (middle), and Σ_{gas} (right) on the x-axis. Shading shows the density of data points in cells of size 0.05 dex wide (in both axes). Green, orange, red, and magenta cells show contours of 1, 2, 5, and 10 sampling points per cell. Individual cells that are not connected and contain only one data point are marked in grey. All data in Figure 4 are at a common resolution of 750 pc.

We plot points from the radial profiles (Figures 2 and 3) on the same plot as black crosses. Generally speaking, the radial profile data lie near the middle of the distribution of the pixel-by-pixel data, as expected. In many cases, features at high Σ_{gas} and high Σ_{SFR} are clearer in the radial profile data because small central rings with high surface densities have small areas and thus contribute only a few individual points to the pixel-by-pixel data.

A common way to parametrize the relationship between star formation and gas is via the gas depletion time or its inverse, the star formation efficiency $\text{SFE} = \Sigma_{\text{SFR}}/\Sigma_{\text{gas}}$. The gas depletion time is the time needed for the present rate star formation to consume the existing gas reservoir. In Figure 4, we plot levels of constant depletion time/SFE as diagonal dotted lines. From bottom to top, these correspond to gas depletion times of 10^{10} , 10^9 and 10^8 years or equivalently depleting 1%, 10% and 100% of the gas reservoir per 10^8 years; these values include helium and so are true depletion times.

3.1. Fits to the Σ_{SFR} Versus Σ_{gas} Distributions

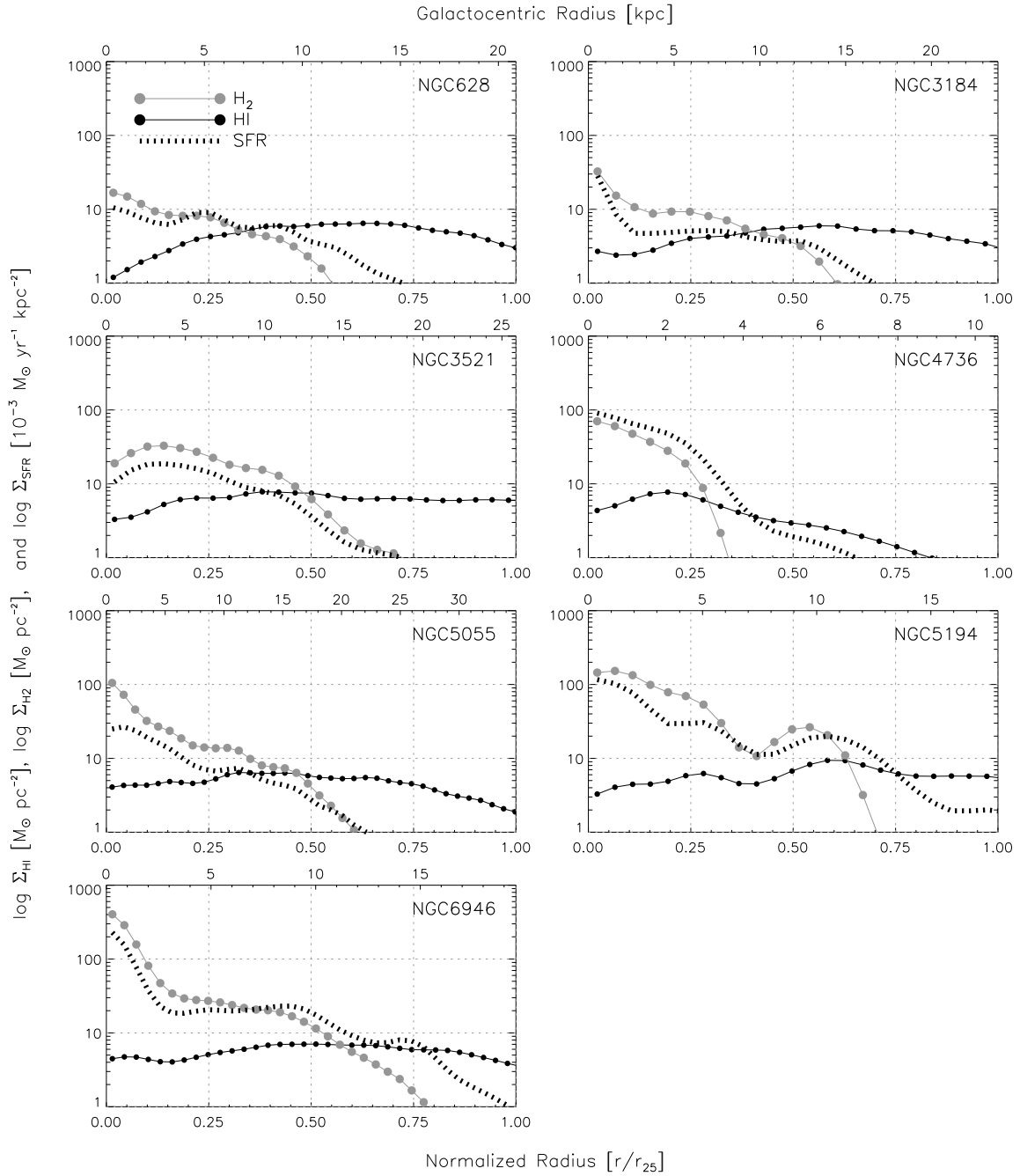


FIG. 2.— Azimuthally averaged radial profiles of Σ_{HI} , Σ_{H_2} , and Σ_{SFR} for spiral galaxies with H_2 -dominated centers. The y -axis shows Σ_{HI} and Σ_{H_2} in units of $M_{\odot} \text{pc}^{-2}$ as well as Σ_{SFR} in units of $10^{-3} M_{\odot} \text{yr}^{-1} \text{kpc}^{-2}$ (the scaling is chosen to bring the profiles onto the same plot). The x -axis shows galactocentric radius normalized by r_{25} (bottom) and in kpc (top). Profiles of Σ_{SFR} and Σ_{H_2} are strongly covariant. Σ_{HI} varies weakly over the optical disk with the main features often being a central depression and a universal upper limit of $\Sigma_{\text{HI}} \approx 9 M_{\odot} \text{pc}^{-2}$.

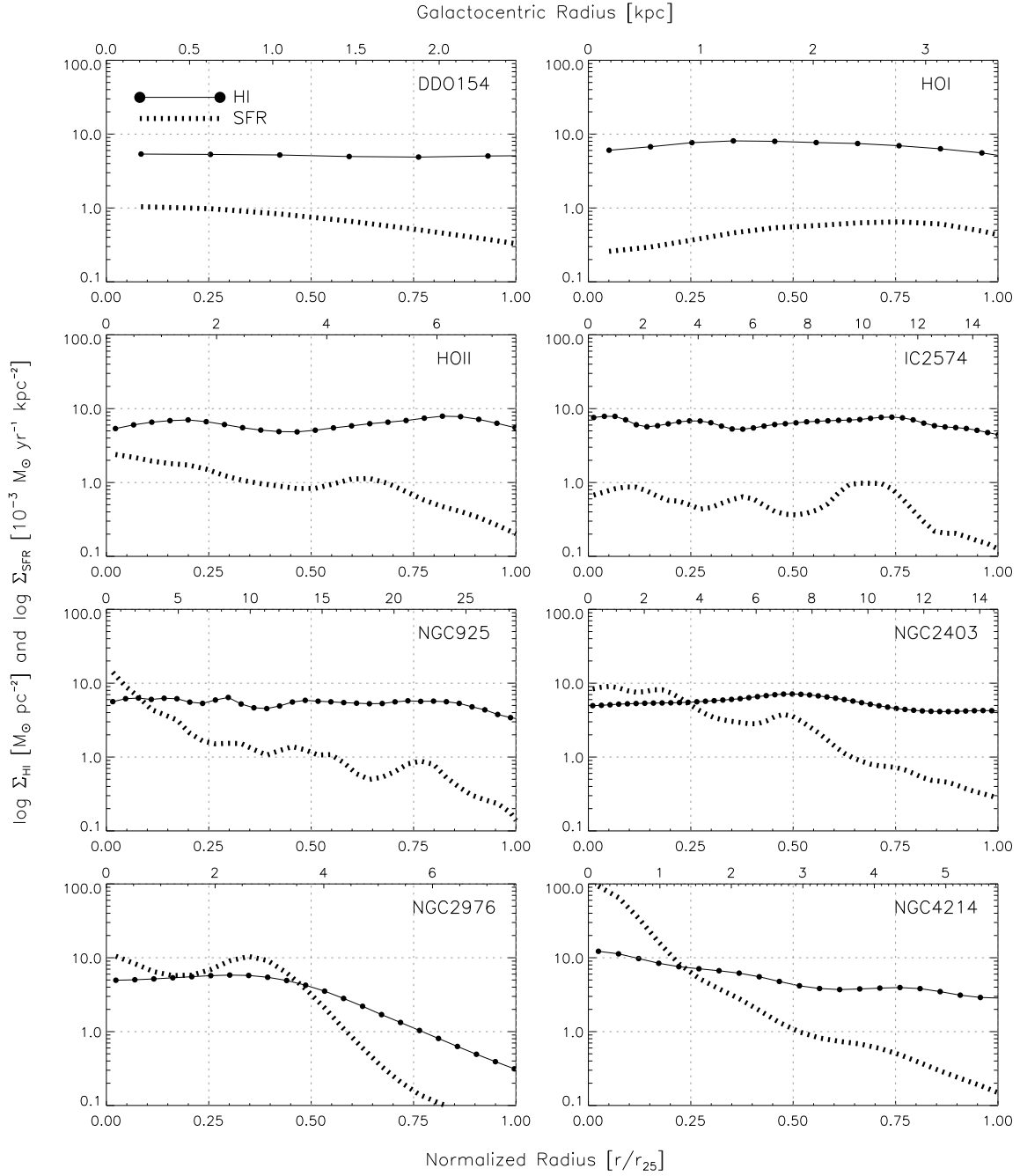


FIG. 3.— Azimuthally averaged radial profiles of Σ_{HI} and Σ_{SFR} for 8 of our 11 HI-dominated galaxies, all late-type spirals or dwarf irregulars. The y -axis shows Σ_{HI} in units of $M_{\odot} \text{pc}^{-2}$ or Σ_{SFR} in units of $10^{-3} M_{\odot} \text{yr}^{-1} \text{kpc}^{-2}$ (the scaling is chosen to bring the profiles onto the same plot). The x -axis shows the galactocentric radius normalized by r_{25} (bottom) and in kpc (top). Σ_{HI} shows the same maximum value seen in spiral galaxies and similarly flat profiles.

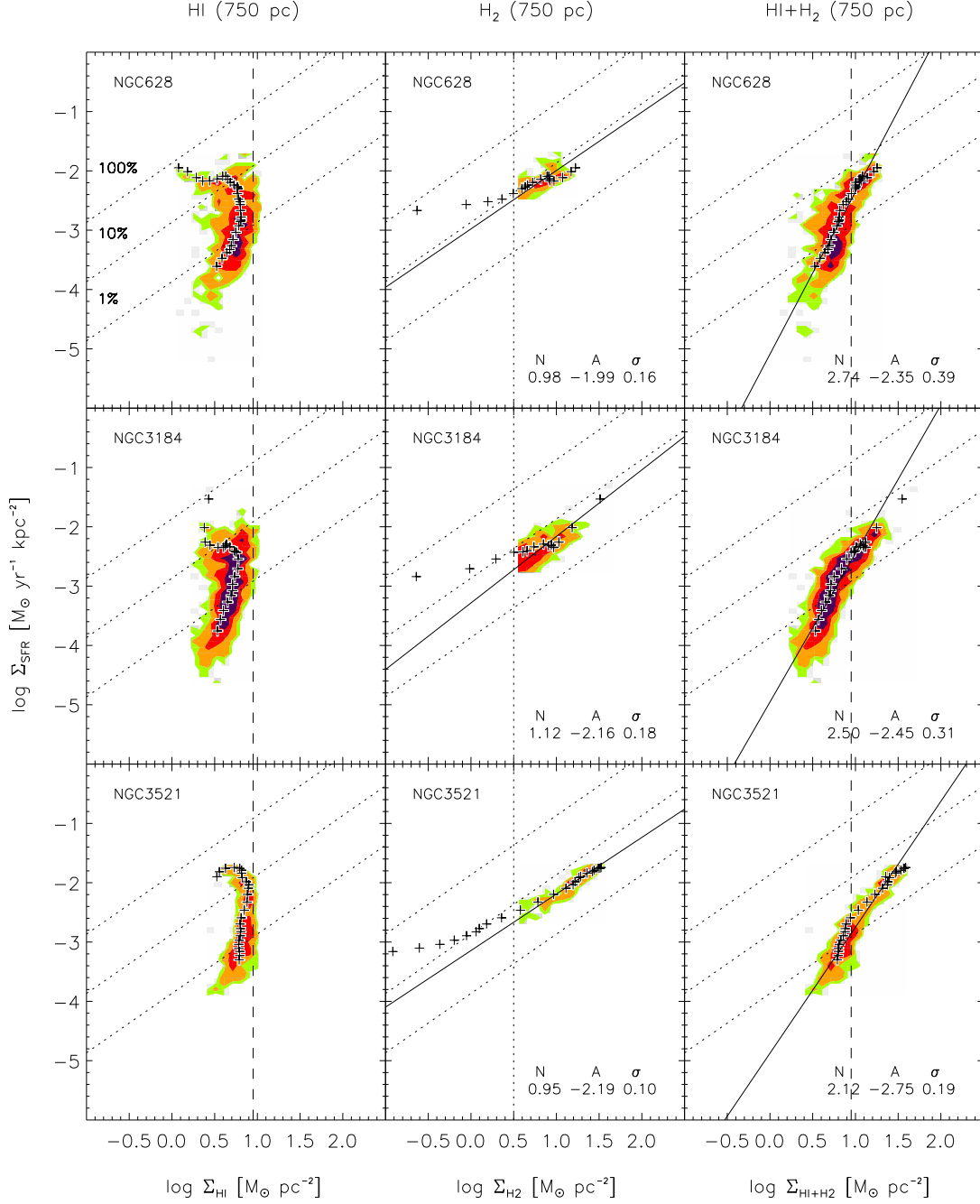


FIG. 4.— Σ_{SFR} as a function of Σ_{HI} (left), Σ_{H_2} (middle), and $\Sigma_{\text{gas}} = \Sigma_{\text{HI}} + \Sigma_{\text{H}_2}$ (right) in our spiral galaxies at 750 pc resolution. Each row shows results for one galaxy. Green, orange, red, and magenta cells show contours of 1, 2, 5, and 10 independent data points per 0.05 dex-wide cell (for H_2 in NGC 4736 we use a scatter plot due to the low number of sampling points.). Crosses show average measurements over tilted rings from the radial profiles. Diagonal dotted lines show lines of constant SFE, indicating the level of Σ_{SFR} needed to consume 1%, 10% and 100% of the gas reservoir (including helium) in 10^8 years. Thus, the lines also correspond to constant gas depletion times of, from top to bottom, 10^8 , 10^9 , and 10^{10} yr. Dashed vertical lines in the HI (left) and total gas (right) plots show the surface density where the HI saturates (see § 3.5). Dotted vertical lines in the middle plots show the typical sensitivity for our CO data. We show OLS bisector fits to the H_2 and total gas data with a solid line and quote the results.

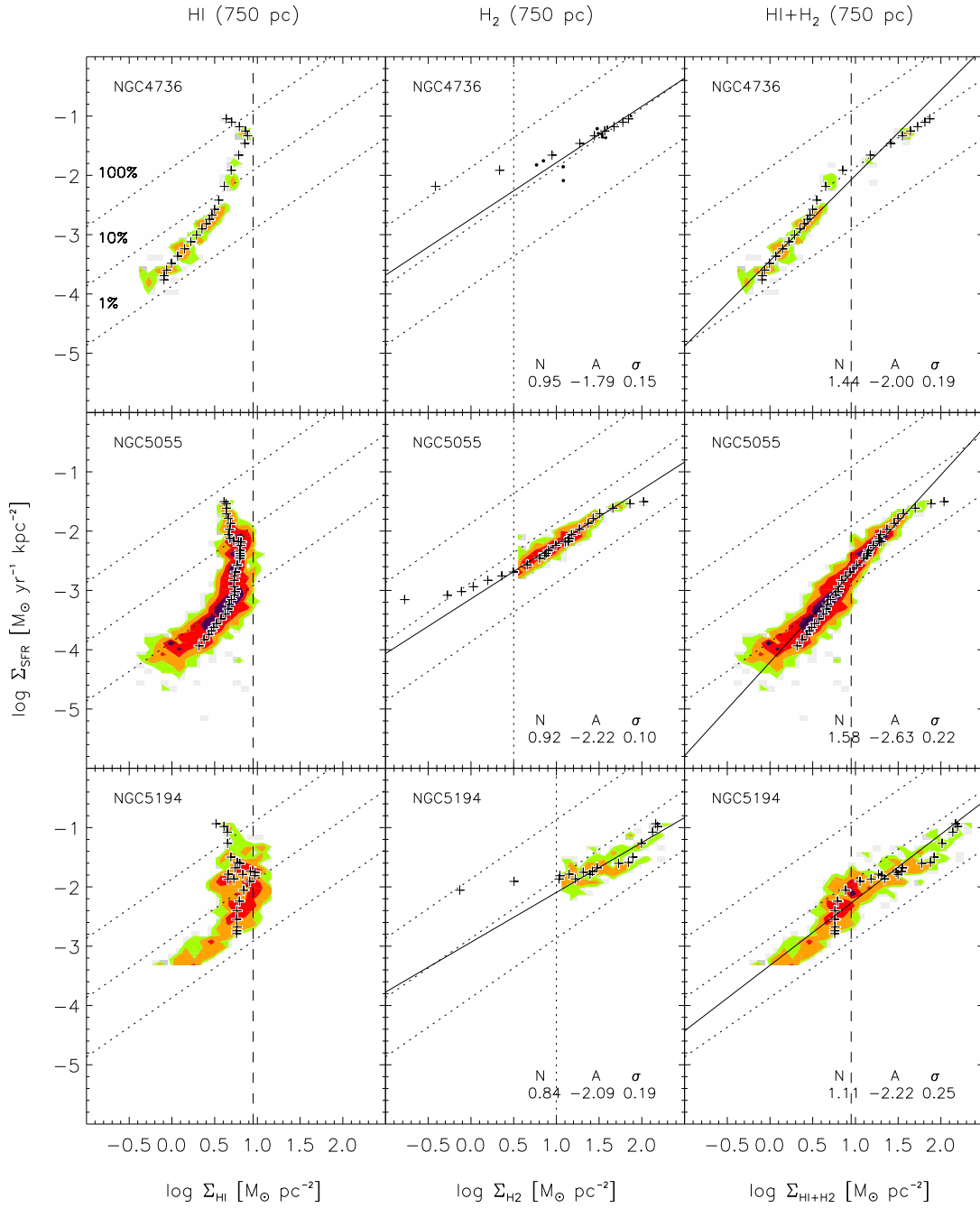


FIG. 4.— continued.

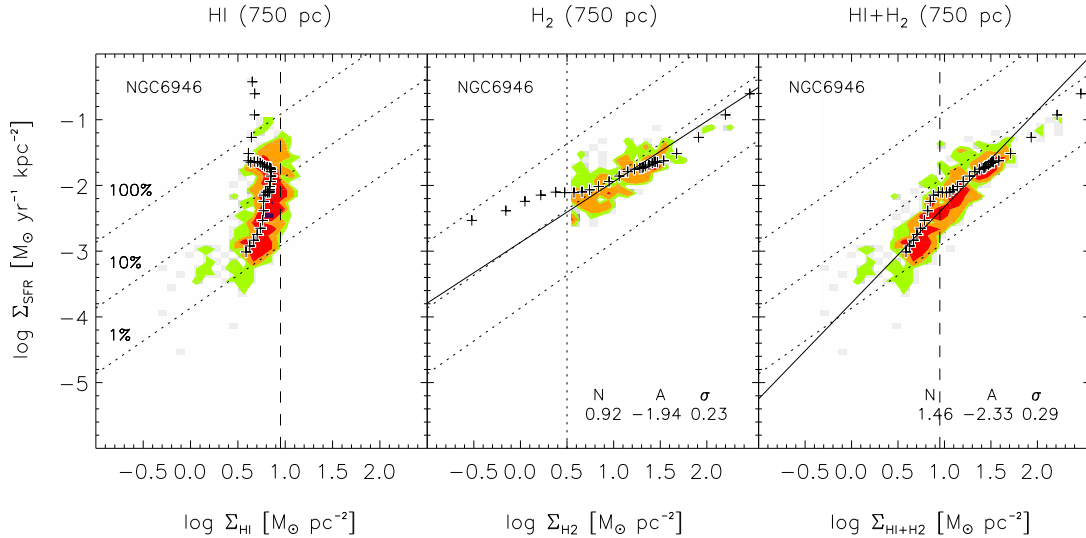


FIG. 4.— continued.

Solid black lines in Figure 4 show the results of fitting a power-law of the form

$$\Sigma_{\text{SFR}} = a \left(\frac{\Sigma_{\text{HI,H2,gas}}}{10 M_{\odot} \text{ pc}^{-2}} \right)^N. \quad (2)$$

using the ordinary least-squares (OLS) bisector. The free parameters are the power law index, N , and a , which is Σ_{SFR} at the fiducial gas surface density of $10 M_{\odot} \text{ pc}^{-2}$. Figure 4 and Table 2 give the best fit values of N , $A = \log_{10} a$, and the RMS scatter in $\log \Sigma_{\text{SFR}}$ about the fit. Because there is not a clear independent variable, we carry out the fit using the OLS bisector (Isobe et al. 1990), giving equal weight to each point. We treat the problem in log space, where fitting a line yields N as the slope and A as the intercept. By centering the fit at $10 M_{\odot} \text{ pc}^{-2}$, a surface density near the middle of the distributions, we minimize the covariance between N and a . We note that readers interested in comparison with previous work should take note of this difference; most fits in the literature quote ‘ A ’ at $1 M_{\odot} \text{ pc}^{-2}$ rather than our fiducial $10 M_{\odot} \text{ pc}^{-2}$.

We fit Σ_{SFR} vs. Σ_{H_2} (middle panel) in the regime $\Sigma_{\text{H}_2} > 3 M_{\odot} \text{ pc}^{-2}$ for the HERACLES data and $\Sigma_{\text{H}_2} > 10 M_{\odot} \text{ pc}^{-2}$ for the BIMA SONG data (see § 2.2.2). These sensitivities are shown as a dotted vertical line in the middle panels of Figure 4. We fit Σ_{SFR} vs. Σ_{gas} to all data points (right panel). The formal errors on the fits are small and the fits are robust to the removal of individual data points. We test the latter via bootstrapping (i.e., repeatedly drawing a new, equal-sized, random subsample from our data allowing repetition) and find the resulting uncertainties to be typically ~ 0.01 in N and ~ 0.05 in A . Methodology, e.g., the decision to fit X vs. Y , Y vs. X , or use of the OLS bisector, drives the resulting fits as much as any other statistical factor. Because both variables are independent, we use the OLS bisector, but estimate the uncertainty by carrying out ordinary least-squares (OLS) fits of Σ_{SFR} vs. Σ_{H} and Σ_{H} vs. Σ_{SFR} . The differences in N and A that we obtain are taken as the uncertainties on the fit. We find that this

brackets the range of reasonable ‘by eye’ fits well. We note that these uncertainties represent only the uncertainty in fitting the distribution of data points. They do not reflect systematics such as uncertainty or variations in the CO-to- H_2 conversion factor, the IMF, etc.

3.2. The Molecular Gas Schmidt Law

Fitting Σ_{SFR} to Σ_{H_2} alone yields power law indices near unity, $N = 0.96 \pm 0.07$ and coefficients $A = -2.06 \pm 0.17$ with a typical scatter of ~ 0.2 dex. That is our 7 spirals display power law indices consistent with an $N = 1$ molecular Schmidt law and only mild variations in the normalization. Another statement of this is that the molecular gas in our sample shows a nearly constant ratio of Σ_{SFR} to Σ_{H_2} that corresponds to star formation consuming the H_2 gas reservoir in $\sim 2 \times 10^9$ yrs (i.e., a constant gas depletion time; also see § 4.3).

3.3. The Total Gas Schmidt Law

The relationship between Σ_{gas} and Σ_{SFR} shows a much larger range of behavior as in the H_2 case. The power law indices, N , for these fits range from 1.11 to 2.74 with the mean 1.85 ± 0.70 and a scatter of ~ 0.3 dex. This range is similar to that found by studies of individual galaxies in the literature ($1 \lesssim N \lesssim 3$, see § 1). These steeper fits, as compared to the H_2 case, are mainly caused by a drop in Σ_{SFR} over a relatively narrow range of gas surface densities just below $\Sigma_{\text{gas}} \sim 9 M_{\odot} \text{ pc}^{-2}$ (see § 3.5 where we assess this further).

There is less variation in the coefficient, A , than in the power law index. A varies from -2.75 to -2.00 with a mean of -2.39 and an RMS scatter of 0.28. This mean value is lower than the mean value for the molecular gas $A = -2.06$ (see § 3.2). The ratio of mean coefficients a for the total gas and the H_2 is ~ 0.3 dex; that is, a particular surface density of molecular gas will on average form stars at about twice the rate of the same surface density of total gas.

It is further evident that there is no universal behavior in the right hand column of Figure 4. That is, the distribution of points in Σ_{gas} - Σ_{SFR} parameter space varies

TABLE 2
FITTED POWER-LAW PARAMETERS AT 750 PC RESOLUTION

Galaxy	Coefficient (A)	H ₂		H I + H ₂		
		Index (N)	Scatter	Coefficient (A)	Index (N)	Scatter
NGC 628	-1.99	0.98	0.16	-2.35	2.74	0.39
NGC 3184	-2.16	1.12	0.18	-2.45	2.50	0.31
NGC 3521	-2.19	0.95	0.10	-2.75	2.12	0.19
NGC 4736	-1.79	0.95	0.15	-2.00	1.44	0.19
NGC 5055	-2.22	0.92	0.10	-2.63	1.58	0.22
NGC 5194	-2.09	0.84	0.19	-2.22	1.11	0.25
NGC 6946	-1.94	0.92	0.23	-2.33	1.46	0.29
Average	-2.06 ± 0.17	0.96 ± 0.07	...	-2.39 ± 0.28	1.85 ± 0.70	...

from galaxy to galaxy. In some cases, e.g., NGC 5194, a single power law appears to relate the two. In other cases, e.g., NGC 3184, Σ_{SFR} and Σ_{gas} are essentially uncorrelated where $\Sigma_{\text{HI}} > \Sigma_{\text{H}_2}$. In these cases, there is no clear one-to-one relationship between total gas and SFR across the whole disk.

What causes some galaxies to display a power law spanning from the H I-dominated to H₂-dominated ISM while others do not? The data-driven answer is that galaxies which show a single power law have comparatively low H I surface densities within their optical disks. Galaxies with uncorrelated Σ_{gas} - Σ_{SFR} distributions (e.g., NGC 3184) by contrast do not have many lines of sight with H I at low surface densities within their optical disks.

One possible explanation is that galaxies with well-defined total gas Schmidt laws (and low H I surface densities) may have lost diffuse H I unassociated with star formation in interactions. Many show signs of tidal disruption or ongoing interactions. Assessing the underlying reason for the range of distributions in the right hand part of Figure 4 is beyond the scope of this paper, the key observation here is that there *is* a range of distributions and that many galaxies are not well described by a single power law relating Σ_{gas} to Σ_{SFR} .

3.4. Star Formation Efficiencies

The SFE provides another way to express the results discussed above. Most galaxies show a fixed SFE relating their Σ_{SFR} and Σ_{H_2} . Some galaxies (e.g., NGC 5194) also show a constant SFE in their total gas spanning from high to low surface densities. The case of NGC 5194 is particularly striking; this galaxy displays a nearly constant SFE spanning surface densities from $1 \text{ M}_{\odot} \text{ pc}^{-2}$ to $100 \text{ M}_{\odot} \text{ pc}^{-2}$. Over two orders of magnitude in gas surface density, the power law index remains near unity and Σ_{SFR} shows only a factor of ~ 2 scatter about a constant SFE.

On the other hand, several galaxies, e.g., NGC 628, NGC 3184 or NGC 3521, show steep distributions in the right hand column of Figure 4 and high power law indices. This may be phrased as large internal variations in their SFE. The variations in SFE are as striking in their own way as the correlation in NGC 5194: these galaxies span nearly an order of magnitude in SFE at an almost constant $\Sigma_{\text{gas}} \approx 5 \text{ M}_{\odot} \text{ pc}^{-2}$. This is clear evidence that the total gas surface density *cannot* be the critical quantity setting the SFR over the H I-dominated parts of these galaxies.

There is also variation in the SFE *among* galaxies. This can be seen from the range of coefficients to our power

law fits. At a particular Σ_{gas} , the average Σ_{SFR} shows an RMS scatter of ~ 0.3 dex. Galaxy-to-galaxy variations thus account for a factor of ~ 2 scatter in the SFE in our sample.

3.5. H I Saturation at High Column Densities

Figure 4 and the radial profiles in Figure 2 also illuminate the relationship between Σ_{HI} and Σ_{H_2} . Both show a striking absence of high surface density H I; this is seen as a sharp right-hand edge to the distributions shown in the left-hand column of Figure 4 and the failure of our radial profiles (spirals or H I-dominated galaxies) to cross $\Sigma_{\text{HI}} \approx 9 \text{ M}_{\odot} \text{ pc}^{-2}$. The only gas in excess of this limiting surface density appears to be in the molecular phase. Wong & Blitz (2002) showed a similar ‘saturation’ effect in azimuthally averaged profiles for their molecular gas-rich spirals, as did, e.g., Martin & Kennicutt (2001) and Morris & Lo (1978). The data plotted in Figure 4 show that this effect is present at 750 pc resolution and that it is remarkably universal. Σ_{SFR} and Σ_{H_2} show no comparable limiting values.

The vertical dashed line in the left and the right columns of Figure 4 shows $\Sigma_{\text{HI, saturation}} \approx 9 \text{ M}_{\odot} \text{ pc}^{-2}$. In Section § 4.1 we will see that 95% of the Σ_{HI} values for the combined distribution of all 7 spiral galaxies in our sample are below $\Sigma_{\text{HI, saturation}}$.

A second effect is best seen in the radial profile points in the left column of Figure 4: at high SFRs there is often an *anti*-correlation between Σ_{HI} and Σ_{SFR} . This occurs in the central H I-holes of spirals where the gas is overwhelmingly molecular and the star formation rate is very high. All 7 of our spiral galaxies show some degree of this effect, i.e., at least a mild central depression in H I.

3.6. Σ_{SFR} Versus Σ_{gas} in H I-dominated Galaxies

We have already seen that there are variations in the relationship between Σ_{gas} and Σ_{SFR} among spiral galaxies, mainly in the H I-dominated parts. Figure 5 shows the relationship between Σ_{SFR} and $\Sigma_{\text{HI}} \approx \Sigma_{\text{gas}}$ for 6 H I-dominated galaxies. Color contours for the two largest galaxies are coded as in Figure 4. For these two galaxies we plot points from the radial profiles (Figures 2 and 3) on the same plot as black crosses. Because the other 4 dwarf galaxies are small, we show scatter plots instead of density contours. Figure 5 shows individual plots for Ho II, IC 2574, NGC 2976 and NGC 4214. Note that the remaining galaxies, Ho I, DDO 154, DDO 53, M81 DwA and M81 DwB are so small that they yield only 1 – 10 sampling points each. We include these data only later

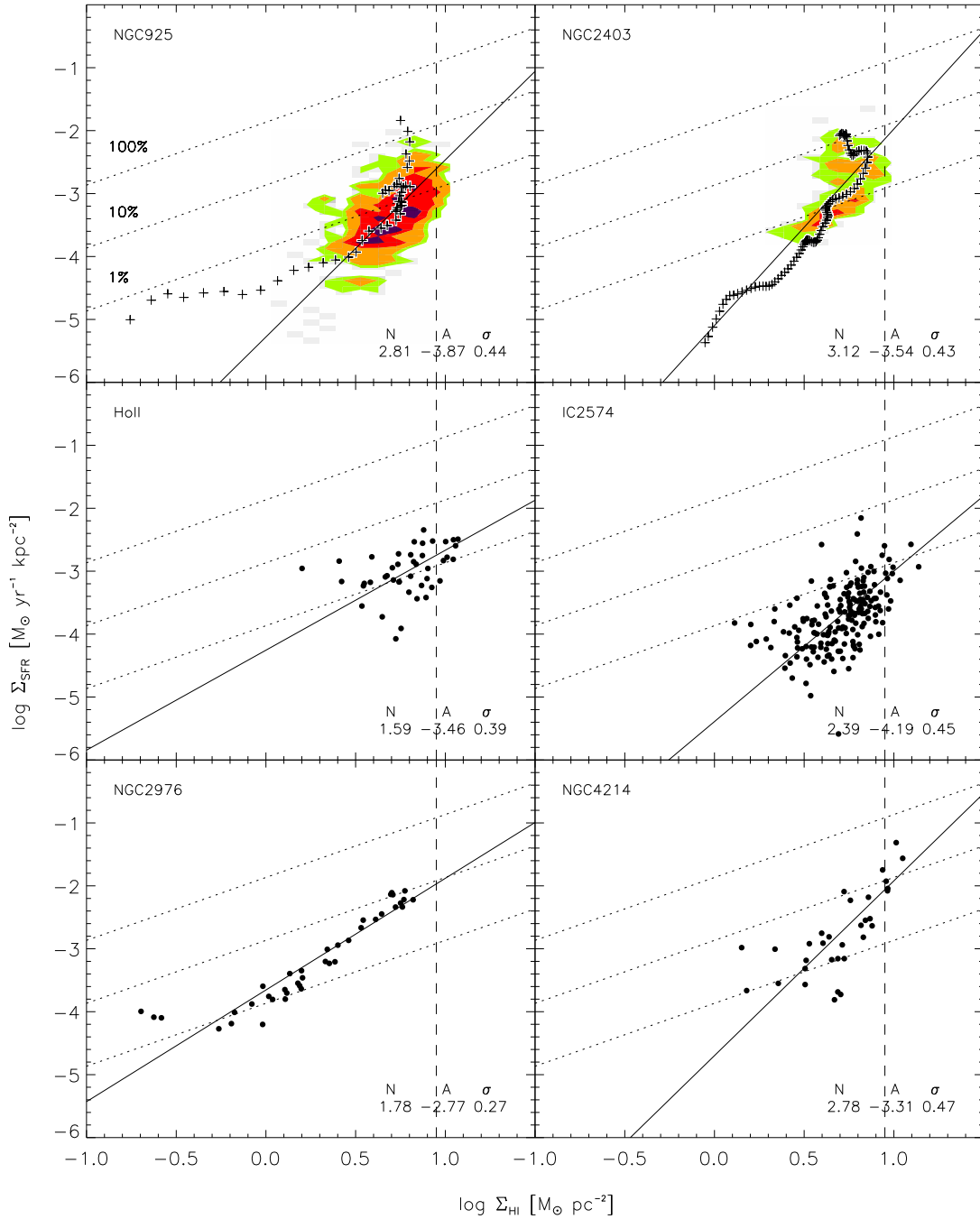


FIG. 5.— Contour and scatter plots respectively of Σ_{SFR} versus Σ_{HI} for 2 H I-dominated spirals and 4 dwarf irregular galaxies at 750 pc resolution. Contour levels, color coding and the dotted diagonal lines of constant SFE are identical to Figure 4. For NGC 925 and NGC 2403, crosses show average measurements over tilted rings from the radial profiles. For the 4 dwarf irregulars we show scatter plots instead of contours due to the lower number of available sampling points. The dashed vertical line indicates the Σ_{HI} saturation level that was found for the spirals.

in Figure 12, which shows aggregate data for all of our dwarf irregular galaxies.

Figure 5 shows that these galaxies display the same saturation value for Σ_{HI} as the large, centrally H_2 -dominated spirals. This is somewhat surprising, as one would expect conditions in the ISM of many of these galaxies to be less favorable to the formation of H_2 from HI because of comparatively low metallicities (and thus lower dust content), shallow potential wells, lower gas densities, and more intense radiation fields. One might therefore have expected large reservoirs of HI to survive in these galaxies at columns where the ISM is mostly molecular in a spiral.

For the most part these galaxies show low SFEs and a steep distribution of Σ_{SFR} as a function of Σ_{HI} . This includes IC 2574, Holmberg II, and all of the ‘small’ irregulars not plotted. The notable exception is NGC 2976, which shows an SFE similar to that found in spiral galaxies and a clear relationship between Σ_{SFR} and Σ_{gas} . As with NGC 4736, this is driven largely by the presence of low gas surface densities in NGC 2976 that are rarely found in the optical disks of many of the other dwarf galaxies. NGC 2976 shows a steadily declining HI profile, perhaps curtailed by interactions with other members of the M81 group.

We know from mapping and single dish measurements that these galaxies are not H_2 -dominated (for a Galactic conversion factor), so Σ_{HI} is likely to be a good proxy for the total gas over most lines of sight. However, if the CO-to- H_2 conversion factor were to vary dramatically, as has been suggested for dwarf irregular galaxies (e.g., Madden et al. 1997; Israel 1997; Leroy et al. 2007), or $\Sigma_{\text{H}_2} > \Sigma_{\text{HI}}$ locally, then Σ_{HI} may severely underestimate Σ_{gas} towards the star forming peaks. The topic is too complex to address here, but we note the sense of the uncertainty: if $\Sigma_{\text{gas}} > \Sigma_{\text{HI}}$, then the points in Figure 5 will move to the right, to higher gas surface densities for the same Σ_{SFR} . Most dwarf irregulars already show lower SFEs than most spiral galaxies; the inclusion of a substantial reservoir of molecular gas would lower the SFE further, thus widening the difference.

3.7. Dependence on Resolution

We have so far considered the relationship between gas and star formation at 750 pc spatial resolution. Cloud formation, stellar feedback, and indeed a breakdown in our SFR tracers may all be strong functions of spatial scale. Therefore we investigate how the relationships between Σ_{SFR} and Σ_{gas} or Σ_{H_2} change with spatial scale. To do this, we convolve all of our data to a variety of spatial resolutions (see §2.3) spanning the range from the original (highest) resolution to 10 kpc and repeat the above analysis.

Figure 6 shows the distribution of Σ_{gas} versus Σ_{SFR} for a range of spatial resolutions in two spiral galaxies, NGC 5194 (M51) and NGC 6946. We show Σ_{SFR} versus Σ_{gas} for 4 spatial resolutions, the original (best) spatial resolution, and then 500 pc, 750 pc and 1 kpc. Contours and other details are identical to Figure 4. Aside from the expected decrease in the number of independent sampling points and some narrowing of the distribution as a result of averaging, we do not observe any strong effect due to spatial resolution.

To look more quantitatively at the effects of resolu-

tion on our results, we fit power laws to the data at each resolution. As noted before, a single power law is an inadequate description of the data for many galaxies; the fits here, however, serve as a shorthand to characterize the data distributions. Figure 7 shows obtained power law parameters as a function of resolution for 6 of our 7 spiral galaxies (star formation in NGC 4736 is too concentrated for this exercise). The fits become more uncertain as the number of sampling points dwindle and averaging substantially lowers our dynamic range for many galaxies. Therefore we can carry out this test between the best available resolution and a spatial resolution of 1 kpc. The left panels in Figure 7 show the power law indices, N , as a function of resolution; the right panels show the power law coefficients, A . For the upper panels, we fit all CO data above the respective sensitivity limit (see §2.2.2). For the bottom panels, we fit all total gas data within $0.4 r_{25}$.

Figure 7 shows that the derived fits change slowly as the spatial resolution decreases from 200 – 500 pc to \sim 1 kpc. If stellar feedback and cloud formation exert a strong influence on the relation between star formation and neutral gas (and indeed one would expect them to) then they do so on scales \lesssim 300 pc. This finding agrees with results from Tamburro et al. (2008), who measured the offset between HI and star forming peaks near spiral density waves in some of the same datasets we study. They found a typical offset of \sim 100 pc or less between regions of star formation and peaks in the HI maps.

4. COMBINED DISTRIBUTIONS

In the previous section we saw that the relationship between Σ_{gas} and Σ_{SFR} varied among spiral galaxies and between spirals and HI-dominated galaxies. We saw that the value at which the atomic gas saturates appears constant across our entire sample and we found a well-defined power law index relating Σ_{H_2} and Σ_{SFR} . In this section we collapse the individual contour plots in Figure 4 into combined pixel-by-pixel plots for all of the galaxies in our sample in order to be able to draw general conclusions about the star formation law in our galaxy sample.

Figure 8 shows the distribution of Σ_{SFR} vs. Σ_{HI} (top left), Σ_{H_2} (top right), and Σ_{gas} (middle right) for all sampling points in our 7 spirals. We also assess the impact of our specific choice of star formation tracer. The bottom two panels in Figure 8 show the relationship between Σ_{SFR} and Σ_{gas} using $\text{H}\alpha$ (bottom left) and, alternatively, a combination of $\text{H}\alpha$ and $24\mu\text{m}$ emission following Calzetti et al. (2007) but here applied pixel-by-pixel (bottom right). The bottom two plots include data for 6 spiral galaxies: NGC 628, NGC 3184, NGC 3521, NGC 5055, NGC 5194, and NGC 6946. All plot parameters are identical to those in Figure 4. In order to turn the $\text{H}\alpha$ and the combination of $\text{H}\alpha$ and $24\mu\text{m}$ emission into SFRs, we assume the same IMF we use for our FUV and $24\mu\text{m}$ based SFR maps. The $\text{H}\alpha$ -only plot furthermore includes a correction for 1.1 magnitudes of extinction for every sampling point (a typical value for integrated galaxy disks, Kennicutt 1998b). The dotted horizontal line in all panels indicates the estimated sensitivity limits for Σ_{SFR} . For ease of comparison, the orange contour from the middle right plot is overplotted as the black contour on both bottom plots.

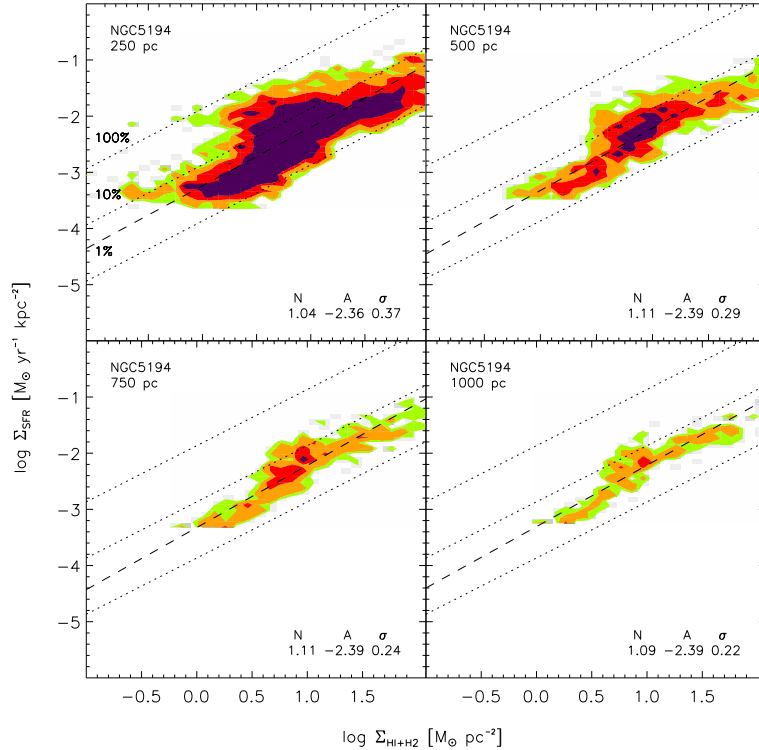


FIG. 6.— Contour plots of Σ_{SFR} versus Σ_{gas} for NGC 5194 (M51) and NGC 6946 at 4 different spatial resolutions: the individual maximum resolution, and then 500, 700 and 1000 pc. Contour levels and other features of the plots, including the diagonal dotted lines of constant SFE, are identical to those in Figure 4. Although the number of independent data points dwindle, we do not see the distribution change markedly with resolution.

One finds that the bottom two distributions in Figure 8, which are based on different SF tracers, agree very well with the distribution that represents the SF tracer used throughout this paper (black contour in bottom panels and middle right panel). That is, our choice of star formation tracer does not appear to significantly affect the derived relationship between Σ_{SFR} and Σ_{gas} .

4.1. HI Saturation in the Combined Distribution

The top left panel of Figure 8 shows Σ_{SFR} vs. Σ_{HI} . This plot clearly demonstrates the saturation effect discussed for the individual galaxies (see §3.5) and shows that it is a universal feature in our sample of spirals. The middle left plot shows normalized histograms of $\log \Sigma_{\text{HI}}$ and $\log \Sigma_{\text{H}_2}$. The HI shows a clear truncation near the threshold. By contrast, the H₂ shows no such cutoff. This indicates that the HI saturation corresponds to a phase transition from an atomic to a molecular ISM. The HI saturation value we quote of $\Sigma_{\text{HI, saturation}} \approx 9 M_{\odot} \text{ pc}^{-2}$ represents the 95th percentile of the HI distribution. This value coincides with the HI saturation value derived from Wong & Blitz (2002) using radial profiles in a sample of 6 molecule-rich spiral galaxies and agrees with our own radial profiles.

4.2. HI, H₂, Total Gas, and the Star Formation Law

The top two panels in Figure 8 show that Σ_{HI} and Σ_{H_2} relate very differently to Σ_{SFR} . In the top left plot, a narrow range of Σ_{HI} corresponds to a large range of Σ_{SFR} and/or SFE. Over less than one order of magnitude in

Σ_{HI} , Σ_{SFR} covers ~ 3 orders of magnitude and the SFE spans 2 orders of magnitude. Σ_{HI} therefore *cannot* be used to predict either Σ_{SFR} or the SFE in spiral galaxies. By contrast, the top right panel shows that Σ_{H_2} exhibits a clear, monotonic relationship with Σ_{SFR} with a slope of approximately unity (see §4.3) down to the sensitivity limit of our CO data.

It is clear from Figure 8 that a single power law *can* describe the relationship between Σ_{SFR} and Σ_{H_2} while the distributions of Σ_{SFR} and Σ_{gas} show a clear ‘knee’ at the transition from an HI to an H₂-dominated ISM.

4.3. The Combined Molecular Schmidt Law

We saw above that the common features in our data are the saturation of the HI and the linear relationship between Σ_{SFR} and Σ_{H_2} . Here we examine this ‘molecular Schmidt law’ for the data from all spiral galaxies combined. In the top left panel of Figure 9 we show the results of a power law fit to Σ_{SFR} vs. Σ_{H_2} for CO data from HERACLES/BIMA SONG in spiral galaxies (where $\Sigma_{\text{gas}} \approx \Sigma_{\text{H}_2}$). Contour levels and other plot parameters are identical to the ones in Figure 4. The power law fit is shown as a solid black line. The best fit parameters are $N = 1.01$ and $A = -2.12$; the RMS scatter of Σ_{SFR} about the fit is 0.19 dex, a factor of ~ 1.5 . In this regime, our data suggest a direct proportionality between Σ_{SFR} and Σ_{H_2} . The derived mean H₂ gas depletion time (including helium) is $2.0 \cdot 10^9$ yrs with an RMS scatter of $0.8 \cdot 10^9$ yrs.

In the middle left panel the CO data comes from BIMA SONG alone. This allows us to plot the data at a slightly

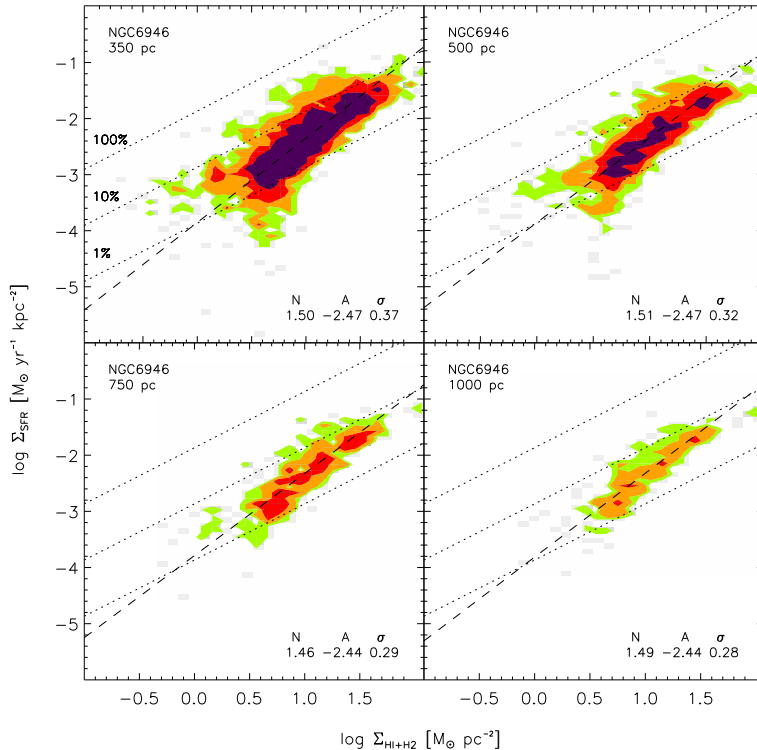


FIG. 6.— continued.

higher resolution of 500 pc and check the robustness of our results to changing CO maps and resolution. All other data and plot parameters are identical to the top left panel. We obtain an identical slope compared to that in the top left panel, $N = 1.03$ versus $N = 1.01$, with a similar coefficient and scatter.

The top and middle right panels show Monte Carlo realizations, where we compute Σ_{SFR} using Σ_{gas} from the data and the fit parameters quoted in the left panels including the measured lognormal scatter. The agreement between the left and right panels provides a qualitative check that a single power law is a good description of our data in this regime.

The bottom left and right panels show how the choice of star formation tracers affects the derived molecular Schmidt law. We use the HERACLES/BIMA SONG maps (at 750 pc resolution) and replace our Σ_{SFR} maps with maps derived from $\text{H}\alpha$ emission (bottom left plot) and a combination of $\text{H}\alpha$ and $24\mu\text{m}$ emission (bottom right plot, Calzetti et al. 2007). The $\text{H}\alpha$ includes a 1.1 magnitude correction for internal extinction. For these data we obtain $N = 1.11$ and $N = 1.18$ respectively. As in Figure 8, the choice of a specific SFR tracer has only marginal impact on our results.

We thus derive a best fit molecular Schmidt law of

$$\Sigma_{\text{SFR}} = 10^{-2.1 \pm 0.2} \Sigma_{\text{H}_2}^{1.0 \pm 0.2}. \quad (3)$$

for the ensemble, identical to within the uncertainties to $N = 1.0 \pm 0.1$ and $A = -2.1 \pm 0.2$ found for individual galaxies (see § 3.1 and § 3.2). The uncertainties of 0.2 take into account variations in SF tracers, substitution of CO maps and scatter in the data. They do not reflect

variations in the CO-to- H_2 conversion factor, the IMF or systematics in our methodology.

5. THE STAR FORMATION LAW AND ENVIRONMENT

We saw above that there are strong variations in the SFE within many spiral galaxies and between spirals and HI-dominated galaxies. In this section we attempt to link variations in the $\Sigma_{\text{SFR}}-\Sigma_{\text{gas}}$ relation outside the H_2 -dominated regime in the spirals to variations in environment. We approach this in two ways: by measuring how the SFE changes with radius within spiral galaxies and by comparing HI-dominated galaxies to spirals.

5.1. The Radial Dependence of the SFE

Our data show that below $\Sigma_{\text{gas}} \approx 9 M_{\odot} \text{pc}^{-2}$, the efficiency with which gas forms stars varies dramatically at a given gas surface density. An obvious explanation is that star formation thresholds of the sort discussed by, e.g., Kennicutt (1989), Martin & Kennicutt (2001), Schaye (2004) or Leroy et al. (2008a) are affecting the relationship between gas and star formation. We sample out to r_{25} and Martin & Kennicutt (2001) find that the last H II region often falls within or near this radius. The thresholds described by various authors stem from a variety of physics. Shear, Coriolis forces, pressure, metallicity, and passage through spiral arms may all play key roles in the formation of gravitationally bound molecular clouds, the necessary prerequisite to star formation.

An exhaustive investigation of all of these other quantities is beyond the scope of this paper but is the topic of a companion paper (Leroy et al. 2008a). However, most of the quantities that have been proposed as critical to

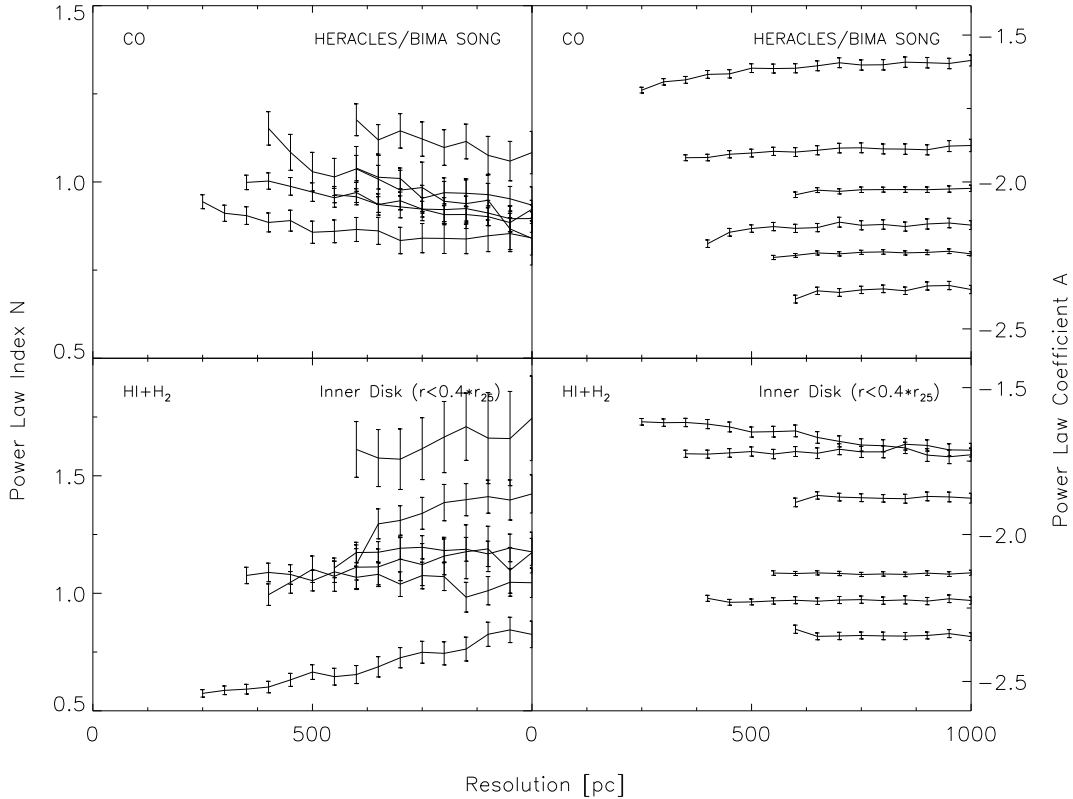


FIG. 7.— Power law fit parameters, power law index N and coefficient A (see Equation 2), for 6 of our 7 spiral galaxies (NGC 4736 is omitted). Left panels: N vs. spatial resolution. Right panels: A vs spatial resolution. The top panels show fits to HERACLES/BIMA SONG CO data, the bottom panels to the total gas data within $0.4 r_{25}$. Both power law parameters vary only weakly with changing spatial resolution.

star formation vary *radially*. Therefore, in Figure 10 we show a scatter plot Σ_{SFR} vs. Σ_{gas} for all 7 spirals. Different colors indicate the galactocentric radius of each sampling point. The plotted data are otherwise identical to the middle right plot in Figure 8. The deprojected galactocentric radius of each point, normalized to the optical radius of the galaxy, determines the color of the point: points within $0.25 r_{25}$ are black; sampling points between 0.25 – $0.5 r_{25}$ are red, those between 0.5 – $0.75 r_{25}$ are orange; and sampling points from 0.75 – $1.0 r_{25}$ are green.

Figure 10 shows that in the centers of spirals, where the gas is mostly molecular, the H_2 depletion time is nearly constant (see § 4.3). At larger radii, where the ISM is dominated by H I , the SFE of gas at a particular surface density depends on the galactocentric radius: The further out in the disk, the lower the SFE.

Figure 11 separates the data from Figure 10 into individual plots of Σ_{SFR} versus Σ_{gas} for specific ranges of galactocentric radius. We use the same radius bins as in Figure 10 and show a separate contour plot for each bin. The upper left panel shows the black sampling points ($< 0.25 r_{25}$) from Figure 10, the upper right plot shows the red points (0.25 – $0.5 r_{25}$), the lower left plot the orange (0.5 – $0.75 r_{25}$), and the lower right plot shows the green sampling points (0.75 – $1.0 r_{25}$). In all plots, we quote the mean SFE in that radius bin and its RMS scatter.

Figure 11 shows that where $\Sigma_{\text{HI}} > \Sigma_{\text{H}_2}$, Σ_{SFR} is a

function not only of Σ_{gas} , but also of local conditions that vary strongly with galactocentric radius. These include, e.g., metallicity, stellar surface density, gas pressure, galactic rotation, and shear. Leroy et al. (2008a) explore the relationship between these quantities, Σ_{SFR} , and Σ_{gas} using the same data we use here.

5.2. H I -dominated Galaxies and the Outer Disks of Spirals

We saw in § 3.6 that the SFE in H I -dominated galaxies is lower than that in spiral galaxies. In the previous section, we showed that the SFE varies dramatically within a spiral galaxy as a function of radius. Here we compare these two findings.

Figure 12 shows the combined distribution of Σ_{SFR} versus Σ_{HI} for all dwarf irregular galaxies in our sample (i.e., the H I -dominated galaxies from Table 1, omitting NGC 925 and NGC 2403 that would otherwise dominate the distribution). We show the same data for the H I -dominated galaxies in all 4 panels. In each panel, we overplot a black contour that shows Σ_{SFR} versus Σ_{gas} for the spiral galaxies from a particular radial bin. This black contour in each panel of Figure 12 corresponds to the lowest (green) contour of the respective panel in Figure 11.

One finds that the distribution of Σ_{SFR} versus Σ_{gas} for the H I -dominated/dwarf galaxies overlaps the distribution of the outer disks of the spiral galaxies (compare bottom right panel of Figure 12). Many conditions are

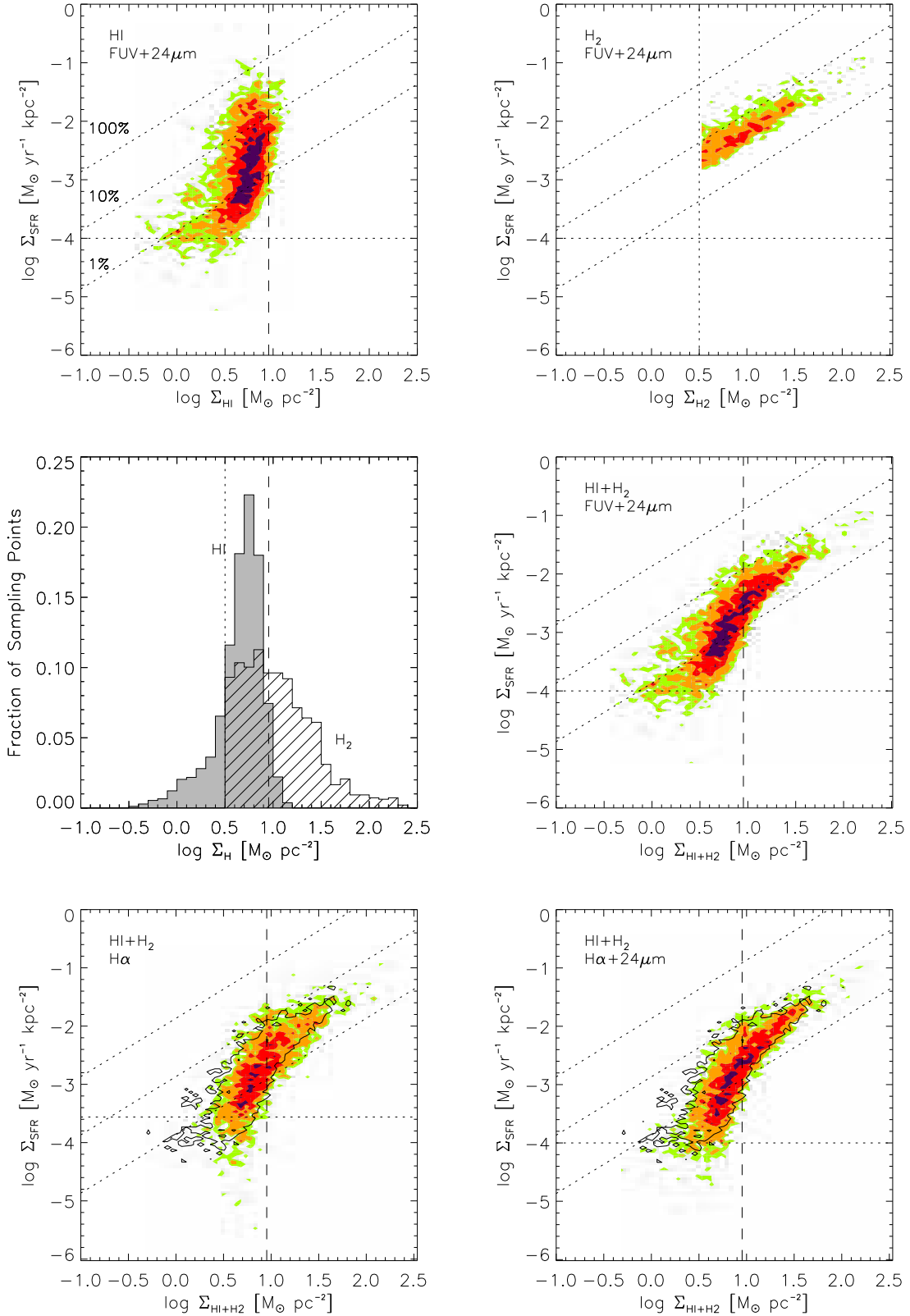


FIG. 8.— Sampling data for all 7 spiral galaxies plotted together. Top left: Σ_{SFR} vs. Σ_{HI} ; top right: Σ_{SFR} vs. Σ_{H_2} ; middle right: Σ_{SFR} vs. Σ_{gas} . The bottom left and right panels show Σ_{SFR} vs. Σ_{gas} using $\text{H}\alpha$ and a combination of $\text{H}\alpha$ and $24\mu\text{m}$ emission as SF tracers, respectively (for a subsample of 6 spirals). The sensitivity limit of each SF tracer is indicated by a horizontal dotted line. The black contour in the bottom panels corresponds to the orange contour in the middle right panel and is shown for comparison. The vertical dashed lines indicate the value at which Σ_{HI} saturates and the vertical dotted lines (top right and middle left panel) represent the sensitivity limit of the CO data. The diagonal dotted lines and all other plot parameters are the same as in Figure 4. The middle left panel shows histograms of the distributions of HI and H₂ surface densities (normalized to the total number of sampling points above the respective sensitivity limit) in the sample.

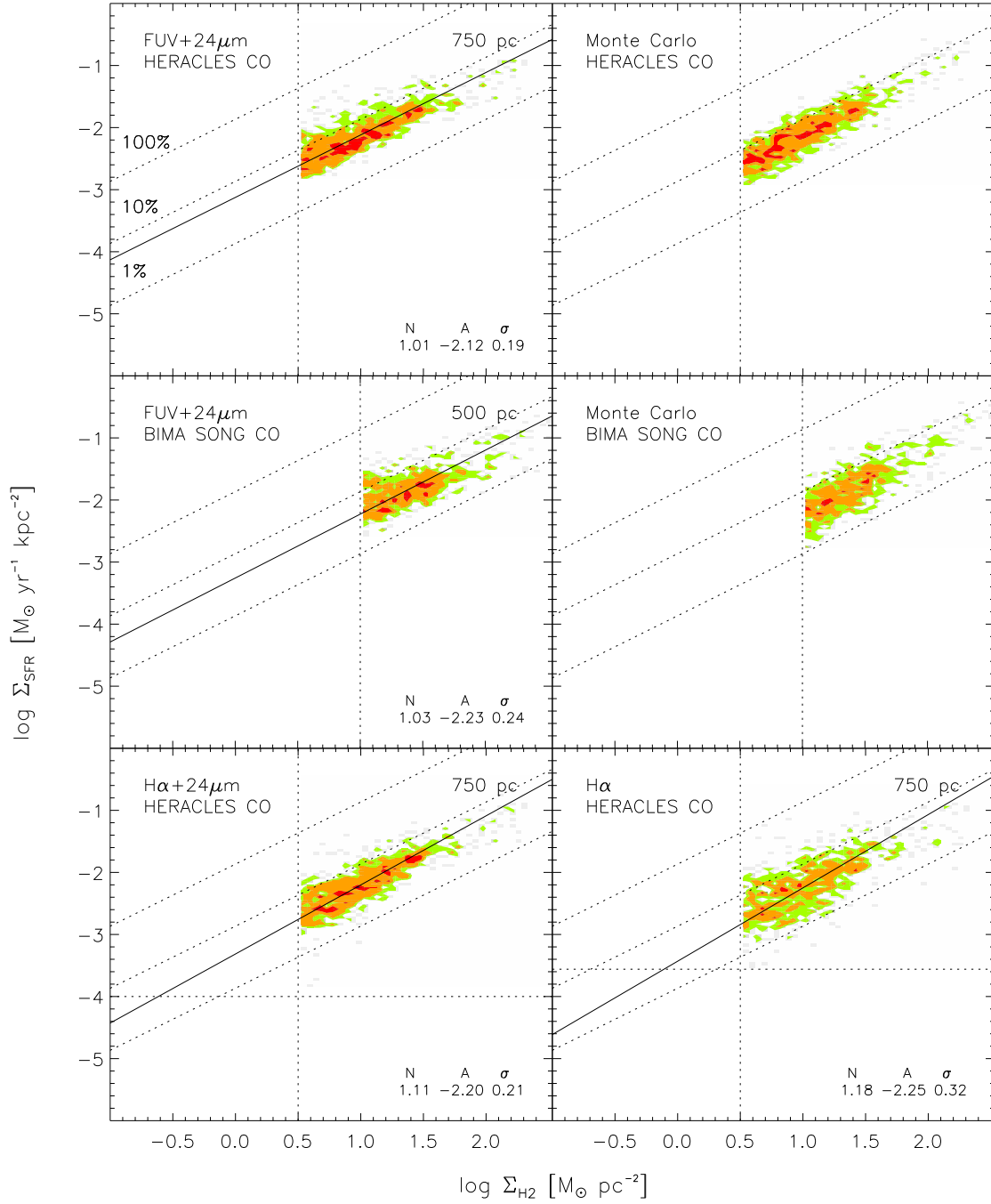


FIG. 9.— The molecular Schmidt law (Σ_{SFR} versus Σ_{H_2}) in spiral galaxies. Green, orange and red cells show contours of 1, 2 and 5 data points per cell. The black solid line shows the best fit power law for every panel. The power law fit parameters are given in every panel. All other lines are the same as in Figures 4 and 8. The top and middle right hand panels show Monte Carlo realizations of the best fit power laws using data values for Σ_{gas} , observed scatter and best fit parameters. All other panels show data distributions.

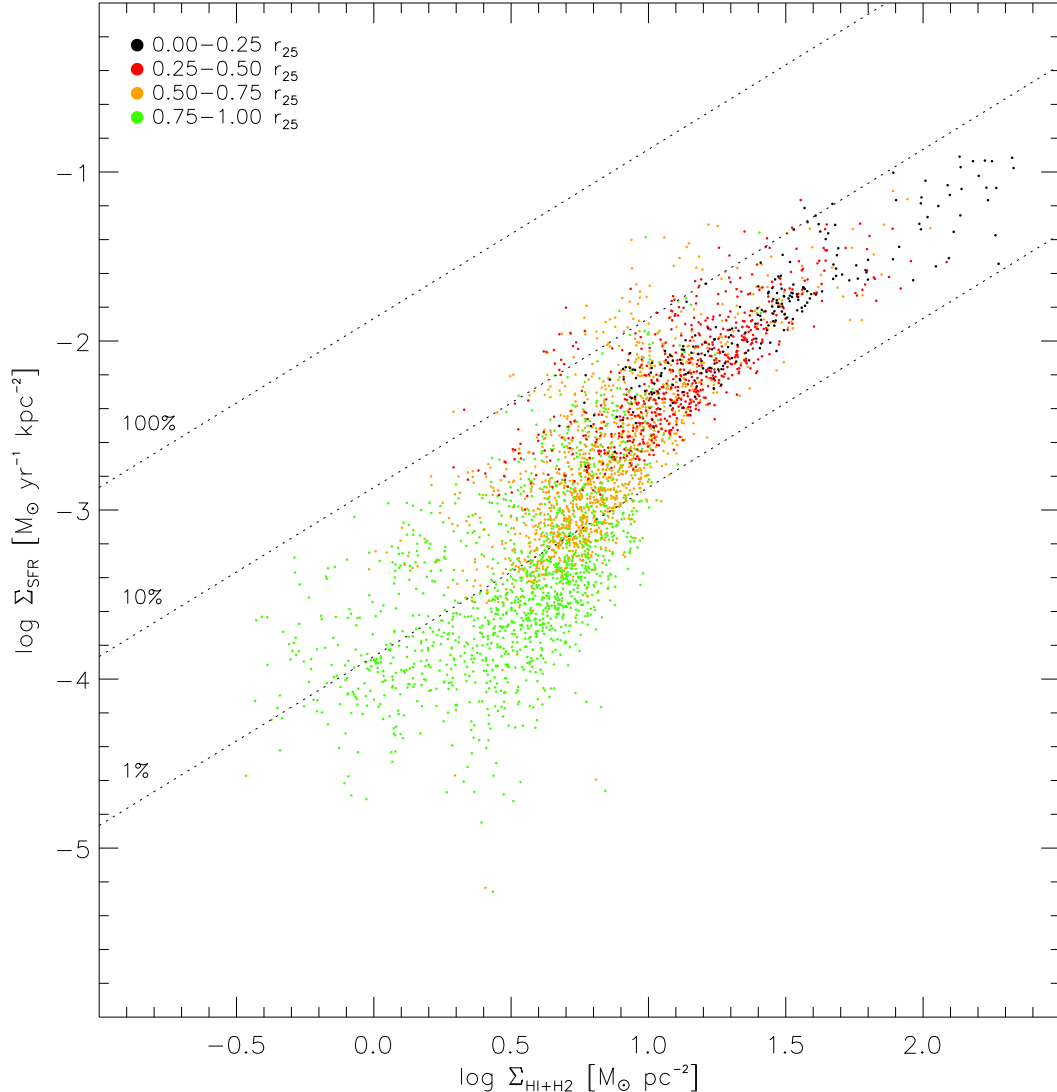


FIG. 10.— Σ_{SFR} versus Σ_{gas} for the spiral galaxies with data colored according to galactocentric radius. Every data point represents one sampling point; the data are the same as in the middle right plot of Figure 8. We show the normalized galactocentric radius of every sampling point via its color, where, in units of r_{25} , the colors correspond to: black < 0.25 ; red $0.25\text{--}0.5$; orange $0.5\text{--}0.75$; and green > 0.75 . The diagonal dotted lines and all other plot parameters are the same as in Figure 4. The data clearly break up according to galactocentric radius, with low SFE/high gas depletion time points corresponding to the outer parts of the spirals.

similar in these two regimes – low metallicities, low dust to gas ratios, high atomic gas fractions, and comparatively weak stellar potential wells. This plot suggests that these shared environmental factors lead to a similar relationship between gas and star formation in both regimes.

We note that one environmental fact that dwarf irregulars do not share with the outer disks of spiral galaxies is differential rotation. Dwarf galaxies tend to have nearly solid body rotation curves and correspondingly low shear, whereas rotation curves tend to be flat in the outer parts of spirals. This implies that shear alone may not be the driving force regulating the SFE.

5.3. The Molecular-to-Atomic Gas Ratio $\Sigma_{\text{H}_2} / \Sigma_{\text{HI}}$ as a Function of Radius

In § 5.1 we saw that where $\Sigma_{\text{HI}} > \Sigma_{\text{H}_2}$, the SFE varies strongly with radius. In combination with our finding that $\Sigma_{\text{SFR}} \propto \Sigma_{\text{H}_2}$ (see § 4.3), this leads us to expect that the $\text{H}_2\text{-to-HI}$ ratio also varies strongly with radius. The right panel in Figure 13 shows $\Sigma_{\text{H}_2} / \Sigma_{\text{HI}}$ as a function of normalized galactocentric radius for all 7 spiral galaxies.

We find that the $\text{H}_2\text{-to-HI}$ ratio decreases as a function of radius. But the sensitivity of our CO data limits the measurement beyond $\sim 0.5 r_{25}$. An alternate approach is therefore to extrapolate Σ_{H_2} from Σ_{SFR} using the direct proportionality between the two that we have established in § 4.3 for the inner part of the optical disk. The FUV and $24\mu\text{m}$ data are more sensitive than our CO maps and so offer more significant measurements in the outer disk. For this approach, we assume that the relationship that we fit between Σ_{SFR} and Σ_{H_2} holds across the disks of our spiral galaxies and infer the ratio $\Sigma_{\text{H}_2} (\Sigma_{\text{SFR}}) / \Sigma_{\text{HI}}$

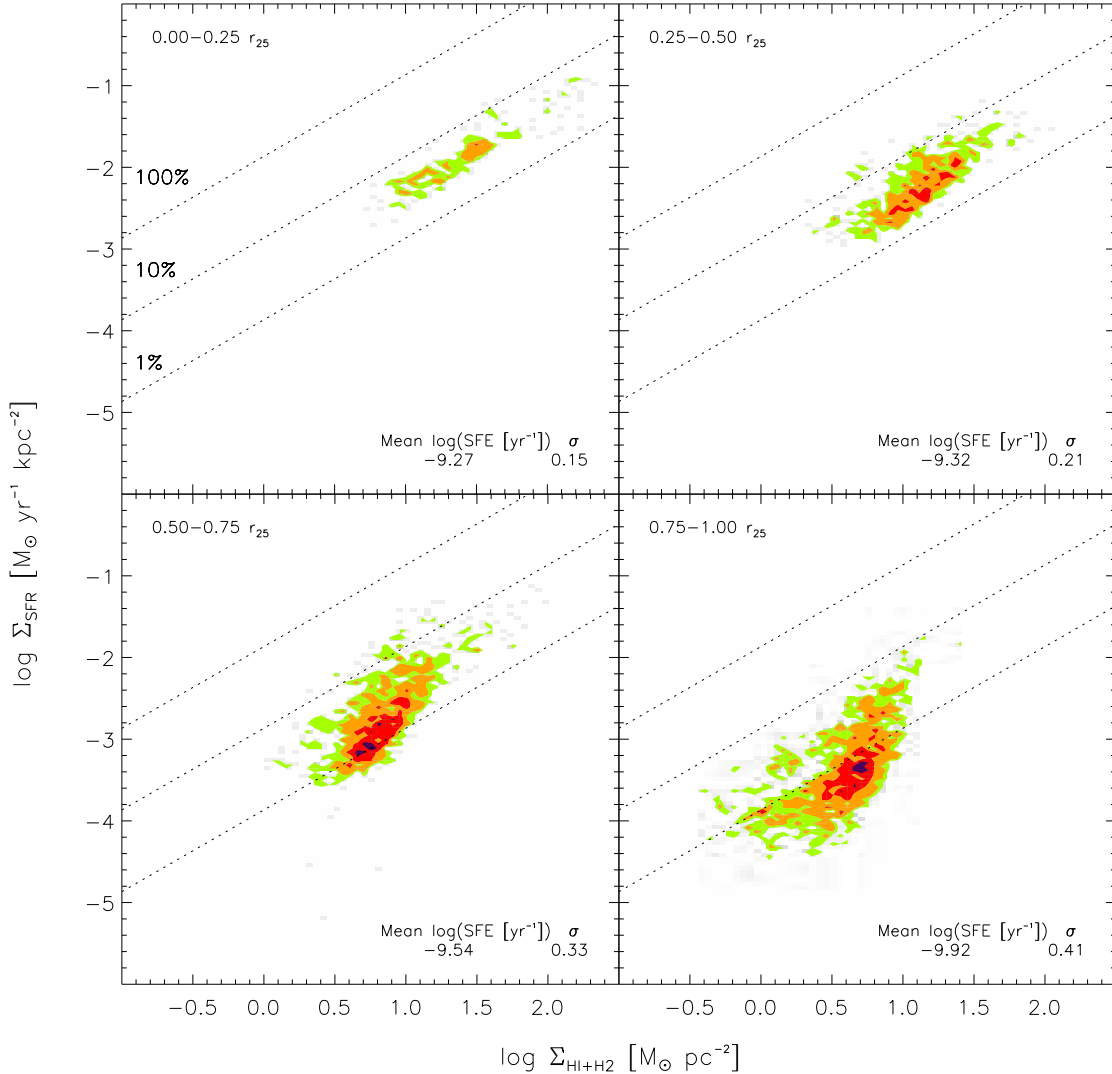


FIG. 11.— The variation of Σ_{SFR} versus Σ_{gas} with radius in spiral galaxies. Levels of 1, 2, 5 and 10 points per cell are shown as green, orange, red and magenta contours. The diagonal dotted lines and all other plot parameters are the same as in Figure 4. Every plot represents only sampling data from a certain range in normalized galactocentric radius, corresponding to a particular color of points in Figure 10. Upper left panel: $< 0.25 r_{25}$ (black points); upper right: $0.25-0.5 r_{25}$ (red points); lower left: $0.5-0.75 r_{25}$ (orange points); lower right: $0.75-1.0 r_{25}$ (green points). Data from outer galaxy disks display lower Σ_{SFR} for the same Σ_{gas} compared to data from the inner disks.

for each sampling point. This is shown in the left panel. For comparison, the green contour in the left panel is overplotted in the right panel as a black contour.

One finds that the two approaches agree reasonably well; the ratio measured from CO overlaps the ratios inferred from Σ_{SFR} . Both panels show that the phase of the ISM is a well-defined function of local conditions that vary with radius. A detailed investigation is beyond the scope of this paper but we explore this topic (often referred to as ‘star formation thresholds’) further in Leroy et al. (2008a). Here we show that an exponential fit, which is shown by the dashed black line in both panels, can provide a good description of the relationship between H_2 , HI and the SFR where $\Sigma_{\text{HI}} > \Sigma_{\text{H}_2}$. The exponential fit yields a scale length of $0.2 r_{25}$ in both panels. The radius where $\Sigma_{\text{H}_2} = \Sigma_{\text{HI}}$ can be derived from the coefficients of the fits. The result is identical in both

cases: $0.43 r_{25}$ in the left panel and $0.46 r_{25}$ in the right panel respectively.

6. SUMMARY & DISCUSSION

6.1. Summary of Our Work

Using data from THINGS, HERACLES, BIMA SONG, the GALEX NGS and SINGS, we derive Σ_{HI} , Σ_{H_2} , and Σ_{SFR} at 750 pc resolution across the optical disks of 7 nearby spiral galaxies with H_2 -dominated centers and 11 HI -dominated late-type galaxies. We use these datasets to make the first pixel-by-pixel analysis of the star formation law in a significant sample of nearby galaxies.

We find two relationships common throughout our data. First, a molecular Schmidt law with index $N = 1.0 \pm 0.2$ relates Σ_{H_2} to Σ_{SFR} in our sample of spirals. This may also be described as a total gas Schmidt law inside $\sim 0.5 r_{25}$, where the ISM of all of our spiral galaxies

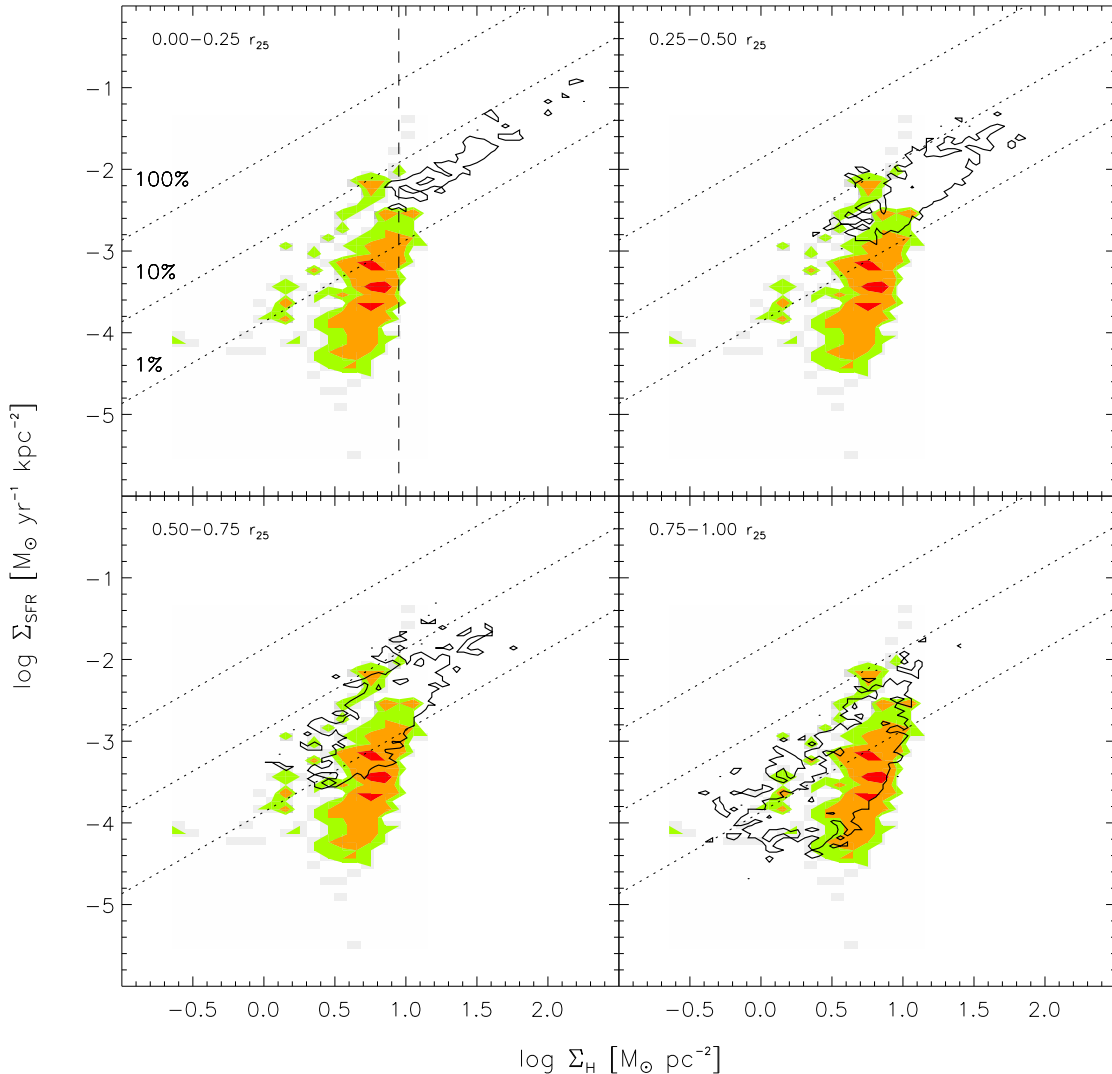


FIG. 12.— A comparison between H I-dominated/dwarf irregular galaxies and different radial regimes of spiral galaxies. All four panels show Σ_{SFR} versus Σ_{HI} for the dwarfs in colored contours. Green, orange, and red contours show 1, 2, and 5 sampling points per cell. The diagonal dotted lines and all other plot parameters are the same as in Figure 4. Overplotted is the lowest (green) contour from the corresponding panel in Figure 11. Thus each panel compares the distribution of data from the dwarfs to that in the spiral galaxies from a particular radial range. The best agreement is seen in the bottom right panel, in which the black contour shows data from $0.75\text{--}1.0 r_{25}$ in spiral galaxies.

is H_2 -dominated. The average molecular gas (including helium) depletion time is $2.0 \cdot 10^9$ years with an RMS scatter of $0.8 \cdot 10^9$ years. This relationship holds for individual galaxies as well as for the combined distribution and is robust to substituting BIMA SONG for HERACLES data, using different SFR tracers, or changing the resolution from ~ 300 pc to ~ 1 kpc.

The second common feature of our data is that Σ_{HI} saturates at a surface density of $\sim 9 M_{\odot} \text{pc}^{-2}$; gas in excess of this value is found in the molecular phase in the spirals. This saturation is common to spiral and H I-dominated galaxies. This is somewhat surprising because conditions in H I-dominated galaxies (such as dwarf galaxies) should be less favorable to the formation of H_2 , which may lead one to expect a higher saturation value; a situation that is not observed.

We do not observe a universal relationship between total gas surface density and Σ_{SFR} . Outside the H_2 -dominated region, i.e., at $r \gtrsim 0.5 r_{25}$, the relationship between gas and star formation varies both within and among galaxies. In some cases, a single power law relates total gas and SFR over many orders of magnitudes in gas surface density. In other cases, we find a wide range of star formation rates at almost the same gas column. As a result of this variation, our best-fit power law index, N , for the total gas in spiral galaxies ranges from 1.1 to 2.7. This agrees well with the range of indices found in the literature, but does not hint at a universal total gas Schmidt law.

We describe variations in the relation between the SFR (Σ_{SFR}) and the total gas (Σ_{gas}) in terms of the star formation efficiency (SFE), i.e., star formation rate per unit gas mass ($\Sigma_{\text{SFR}}/\Sigma_{\text{gas}}$), and the H_2 -to-H I ratio

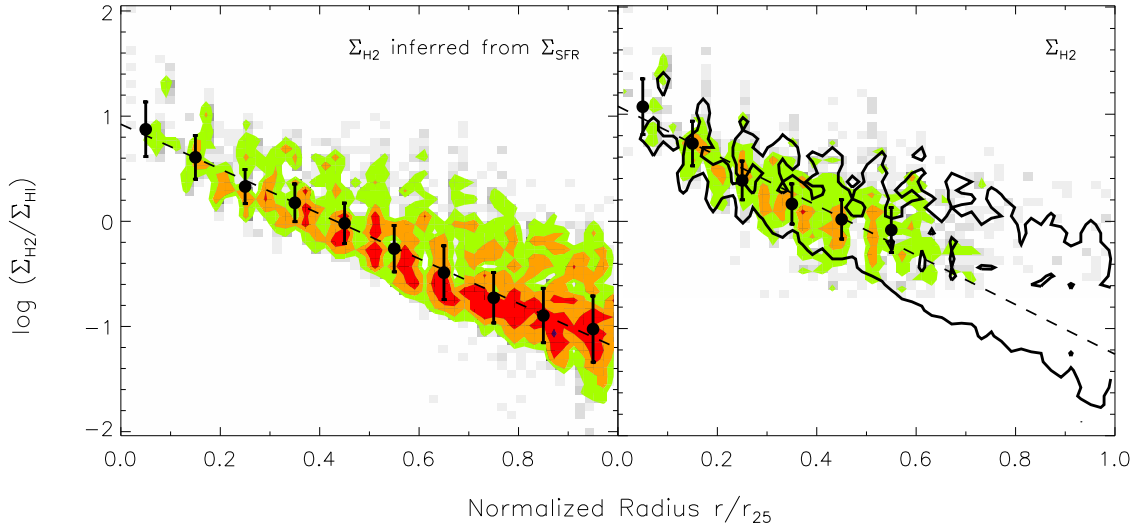


FIG. 13.— The ratio of molecular to atomic gas, $\Sigma_{\text{H}_2} / \Sigma_{\text{HI}}$, as a function of galactocentric radius for the spiral galaxies. In the left panel, Σ_{H_2} is inferred from Σ_{SFR} using the direct proportionality between the two that we have established in § 4.3. In the right panel, Σ_{H_2} from HERACLES is used directly. The black contour in the right panel is identical to the green contour in the left panel and is shown for comparison. Green, orange, and red cells show contours of 2, 5 and 10 sampling points per cell (cell sizes: $\Delta x = 0.02 r_{25}$, $\Delta y = 0.08 \text{ dex}$). The filled black circles show the median Σ_{SFR} per $0.1 r_{25}$ radial bin, the error bars represent the 1σ scatter in each bin. We carry out exponential fits to both distributions (dashed black lines).

($\Sigma_{\text{H}_2}/\Sigma_{\text{HI}}$). We show that outside of the central, H_2 -dominated regime of spiral galaxies, the SFE has a strong gradient with radius, where the highest efficiency points come from the inner disk, and the lowest efficiency points are at larger radii. We also show that the pixel-by-pixel distributions of late-type, HI -dominated galaxies overlap those of the outer disks of the spirals in our sample in $\Sigma_{\text{SFR}}-\Sigma_{\text{gas}}$ parameter space. This implies that similar conditions, i.e., low metallicities, weak potential wells and low dust content, might drive the SFE in this regime.

We argue that these observations show a clear link between environment and the relationship between gas and star formation. We suggest the following scenario: the observational star formation ‘law’, as it is now understood (e.g., K98), is a molecular phenomenon. The transition from HI to H_2 and the subsequent formation of stars is not purely a function of the total gas surface density. Instead, other physics sets the ratio of HI to H_2 . The critical quantity for these processes is a strong function of radius and appears to be common to both dwarf irregular galaxies and the outer regions of spiral disks. This agrees quantitatively with the findings of Wong & Blitz (2002) and qualitatively with the ideas of star formation thresholds discussed by, e.g., Kennicutt (1989), Martin & Kennicutt (2001), Leroy et al. (2008a) and many others.

We test these results in several ways and find that our conclusions are robust against variations in the star formation rate tracer used or the applied spatial resolution. Moreover, we find the same results when performing a pixel-by-pixel analysis and when working with azimuthally averaged radial profiles.

6.2. Comparison with Previous Measurements

As we discussed in § 1, many different studies have examined the SF law in nearby galaxies and derived a variety of power law indices. These studies have used a wide

range of SFR tracers, methodologies (disk averaged measurements, radial profiles or individual apertures) and assumptions (e.g., adopted IMF or CO -to- H_2 conversion factor). Here we compile the results from several studies whose galaxy samples overlap our own to compare the data distributions in $\Sigma_{\text{SFR}}-\Sigma_{\text{gas}}$ phase space once different methodologies are accounted for.

In Figure 14, we therefore compare our Σ_{SFR} vs. Σ_{gas} pixel-by-pixel distributions and our radial profile data to measurements from other authors after matching the assumptions which have gone into each of their analyses to ours. In each panel, the colored contours represent the pixel-by-pixel data from our study; these distributions are identical to the ones in Figure 4. The black crosses represent the datapoints from our radial profiles (Figure 2) and are also identical to the crosses in Figure 4.

The black dots in Panel A and the black circles in the other panels show data from previous papers. These data were adjusted to match our assumptions regarding the adopted IMF (see § 2.3.2), the inclination, the CO -to- H_2 conversion factor, and the $I_{\text{CO}}(J=2 \rightarrow 1)/I_{\text{CO}}(J=1 \rightarrow 0)$ line ratio. We mention the adjustments that were made for each dataset in the discussion of the individual panels of Figure 14 below.

Panel A: Kennicutt et al. (2007, K07) derive a power law index of 1.37 ± 0.03 relating molecular gas and SFR surface densities in M51 (and an index 1.56 ± 0.04 for the total gas). They measure Σ_{gas} and Σ_{SFR} by placing 520 pc apertures on $\text{H}\alpha$ and $24 \mu\text{m}$ emission peaks (black dots in Panel A in Figure 14). K07 use $\text{Pa}\alpha$ and a combination of $24 \mu\text{m}$ and $\text{H}\alpha$ emission to estimate Σ_{SFR} . They use the same HI and CO data we do.

Shown (Figure 14 A) is a comparison for NGC 5194 (M51) between our data and the measurements from K07, which we have adjusted to match our CO -to- H_2 conversion factor and IMF. One finds that our data distribution generally agrees quite well with that from

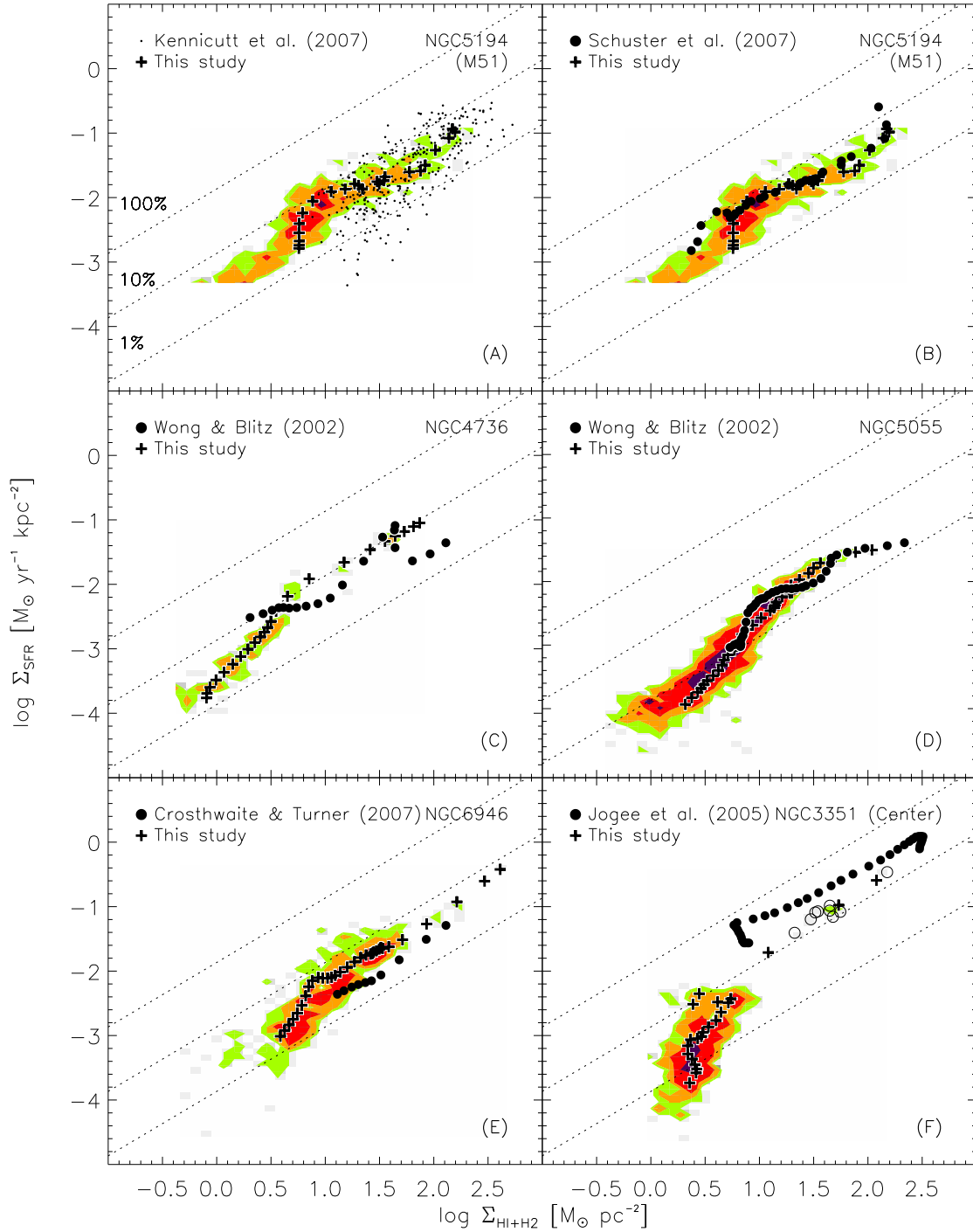


FIG. 14.— Σ_{SFR} versus Σ_{gas} for individual galaxies from this study and from previous analyses. The colored contours represent the pixel-by-pixel data for spiral galaxies from this study; the distributions are identical to the respective ones in Figure 4. The diagonal dotted lines and all other plot parameters are the same as in Figure 4. Overplotted are datapoints from our radial profiles (compare Figures 2 and 4) as black crosses. We compare our data to measurements from other analyses, which were carried out either by using individual apertures (panel A; each black dot represents the measurement within an individual aperture) or radial profiles (other panels; each filled black circle represents a radial profile data point). The references are given in each panel. We adjust these data to match our adopted inclinations, IMF, CO line ratio and CO-to-H₂ conversion factor. In general, there is good agreement between our data and the measurements from other studies, but the comparison also shows that the distributions are quite sensitive to some of the underlying assumptions, e.g., how one corrects for extinction or which CO-to-H₂ conversion factor is applied.

K07. Nevertheless, the regime that both studies probe is slightly different: whereas we sample the entire optical disk, K07 focus on apertures mainly in the spiral arms of M51. As a consequence, our data distribution extends to lower Σ_{gas} while their distribution emphasizes slightly higher Σ_{SFR} and Σ_{gas} .

The power law slope of 1.37 ± 0.03 derived in K07 for the molecular gas is steeper than the value of 0.84 that we derive for M51 (see Figure 4 and Table 2). The steeper slope in K07 is driven mainly by the fact that they measure low Σ_{SFR} for some apertures at $\log(\Sigma_{\text{gas}})$ between ~ 1 and 1.8 (compare black points in panel A). This difference arises because K07 subtract a local H α and 24 μm background for each aperture. This has marginal impact at high Σ_{SFR} , but significantly affects low Σ_{SFR} measurements where the contrast with the local background is low. This comparison shows that despite using the same gas data and similar SFR tracers, the applied methodology for deriving SFRs and the specific choice of sampling method have non-negligible impact on the derived power law slopes.

In *Panel B* we compare our M51 distribution to data adopted from Schuster et al. (2007), which are adjusted to match our $I_{\text{CO}}(J=2 \rightarrow 1)/I_{\text{CO}}(J=1 \rightarrow 0)$ line ratio, IMF and CO-to-H $_2$ conversion factor (we note that they apply a conversion factor equal to one quarter of our adopted value). Schuster et al. (2007) use radial profiles and obtain a power law index of 1.4 ± 0.6 when fitting SFR and total gas surface densities in M51. They use radio continuum emission at 20 cm to derive Σ_{SFR} .

In this panel, we plot their data after adjusting for differences in the applied line ratio, IMF and CO-to-H $_2$ conversion factor and find good agreement for the distributions. The discrepancy at small Σ_{gas} arises because the HI data used in Schuster et al. (2007) are less sensitive than our map. This leads to decreasing HI columns at larger radii in their radial profile while our profile remains flat. The central radial profile point from Schuster et al. (2007) shows a particularly high Σ_{SFR} . This may be due to the AGN in M51, which is a strong source of radio continuum emission.

Panel C and D: Both panels show radial profile data adopted from Wong & Blitz (2002), panel C for NGC 4736 and panel D for NGC 5055. In both panels, the data from Wong & Blitz (2002) are adjusted to match our IMF and adopted inclinations. They derive their SFRs from H α emission and for their plotted datapoints in Panels C and D, we have adopted their constant global extinction correction of 1.5 mag. We note that the radial profiles from Wong & Blitz (2002) only extend out to $\sim 150''$ and $\sim 300''$ for NGC 4736 and NGC 5055, respectively, while ours reach the edge of the optical disks ($\sim 230''$ and $\sim 350''$, respectively).

For NGC 4736, the observed Σ_{SFR} for the Wong & Blitz (2002) profile are lower than those measured by us (apart from their ‘bump’ at $\log(\Sigma_{\text{gas}}) \approx 1.5$). For this galaxy, their derived Σ_{SFR} depends sensitively on the method used to correct the H α emission for extinction: mid-IR (24 μm), fixed extinction, and a gas column based extinction estimate yield results that differ by a factor of about two. In the case of NGC 5055 (Panel D), the agreement between both distributions is excellent for all Σ_{gas} .

Panel E compares data for NGC 6946 adopted

from Crosthwaite & Turner (2007), adjusted to match our adopted inclination and IMF, to our data. Crosthwaite & Turner (2007) use radial profiles and find a proportionality between the molecular gas and the SFR surface density (implying a power law slope of ~ 1 for the molecular gas). They derive their SFRs from FIR and radio continuum emission. We will, however, only use the FIR based SFRs in our comparison, because it is easier to match assumptions for this case. Our radial profile extends to larger radii (and thus includes lower Σ_{gas} values) and because Crosthwaite & Turner (2007) average emission in $30''$ wide rings (our study: $10''$), they have fewer datapoints and their Σ_{SFR} and Σ_{gas} show less dynamical range. Despite an offset in Σ_{SFR} , likely due to the different SFR tracers, both distributions are in good qualitative agreement.

Panel F: We compare pixel-by-pixel data from NGC 3351, which is not part of our current sample, to inner disk data from Jogee et al. (2005). Their data are adjusted to match our IMF, CO-to-H $_2$ factor and adopted inclination (41°). They use radial profiles to sample the inner 1 kpc of NGC 3351. Because they restrict their analysis to the inner disk, they only consider molecular gas. They derive their SFRs from Br γ emission. This comparison allows us to study a regime of relatively high Σ_{SFR} and Σ_{gas} . Due to the coarser resolution of our data (750 pc) compared to the data from Jogee et al. (2005, 120 pc for NGC 3351), we can only compare 3 radial profile points (black crosses) and a few individual pixel-by-pixel sampling points (highlighted as black circles) to the measurements of Jogee et al. (2005, black filled circles). We find an offset in terms of Σ_{SFR} , probably due to the different SFR tracers used. Both distributions show good qualitative agreement nevertheless.

These comparisons show that once the different assumptions of all measurements are accounted for, the data distributions from the different studies agree well in general. This appears to be relatively independent of the specific SFR tracer or the sampling method (e.g., pixel-by-pixel or radial profiles) that is applied. The resolution of the data seems to matter only marginally, as, even when disk averaged measurements are included, the data still populate the same regime in $\Sigma_{\text{SFR}}-\Sigma_{\text{gas}}$ phase space (as we will discuss in § 6.3).

When one corrects for different assumptions, the CO-to-H $_2$ conversion factor is especially important and matters particularly in the inner part of galaxies, where the molecular gas dominates the total gas budget. The factors originally applied in the above studies differ by as much as a factor of 6. If one does not correct for different conversion factors, the high Σ_{gas} end of the distributions may change quite drastically, which can significantly influence derived power law slopes.

Nuclear activity, i.e., the presence of AGN, may also play a role for radial profile datapoints from the centers of galaxies, depending on the applied SFR tracers (see discussion for Panel B). This is only a minor issue when sampling pixel-by-pixel, where only very few pixels from the center contribute.

6.3. The Molecular Schmidt Law In Various Regimes

Figure 15 shows our combined pixel-by-pixel distribution together with all the literature measurements dis-

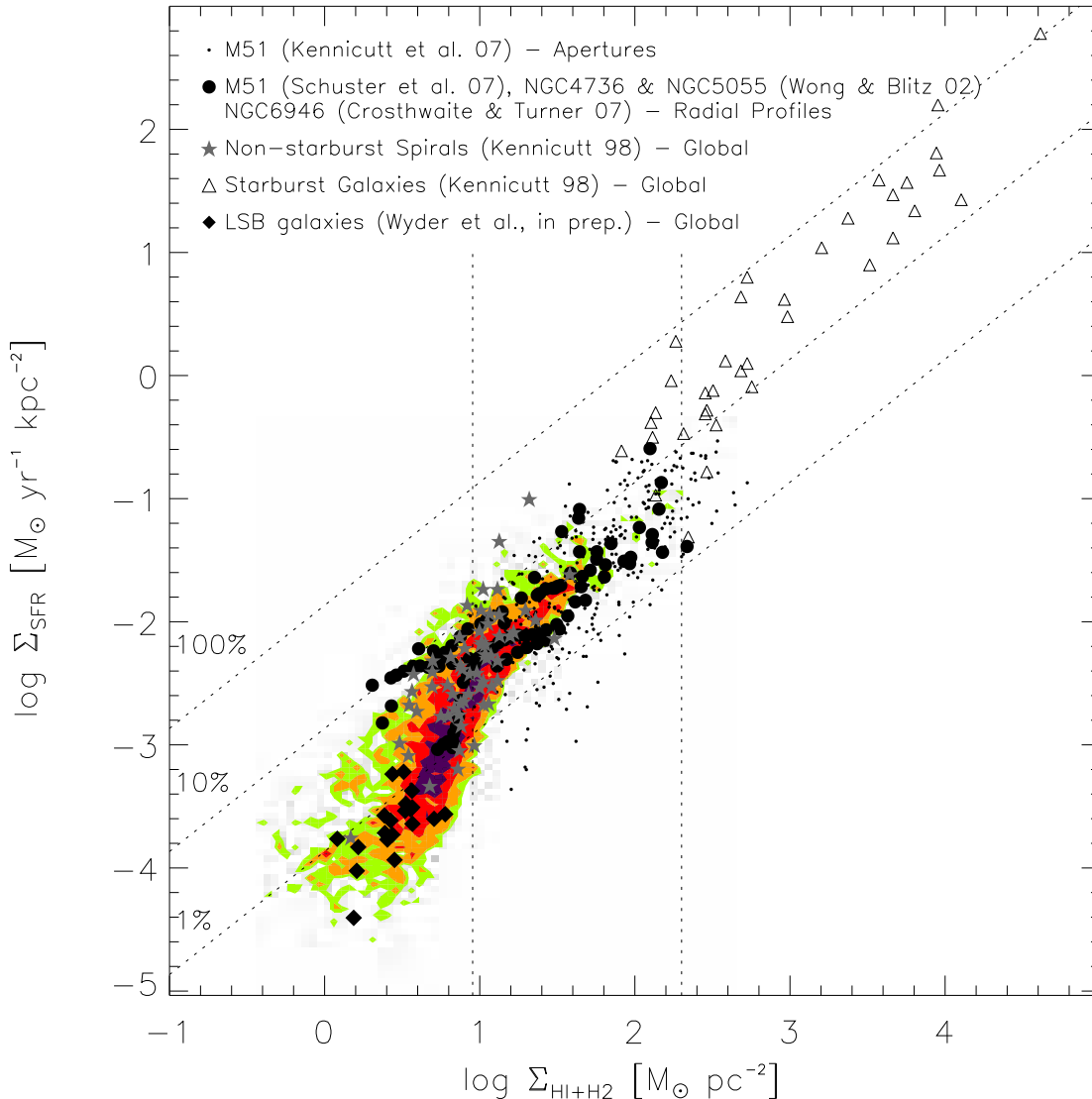


FIG. 15.— Σ_{SFR} versus Σ_{gas} from this paper in colored contours (compare middle right panel of Figure 8) and for individual galaxies from other analyses (see Figure 14). The diagonal dotted lines and all other plot parameters are the same as in Figure 4. Overplotted as black dots are data from measurements in individual apertures in M51 (Kennicutt et al. 2007). Datapoints from radial profiles from M51 (Schuster et al. 2007), NGC 4736 and NGC 5055 (Wong & Blitz 2002) and from NGC 6946 (Crosthwaite & Turner 2007) are shown as black filled circles. Furthermore, we show disk averaged measurements from 61 normal spiral galaxies (filled grey stars) and 36 starburst galaxies (triangles) from K98. The black filled diamonds show global measurements from 20 low surface brightness (LSB) galaxies (Wyder et al., in prep.). Data from other authors were adjusted to match our assumptions on the underlying IMF, CO line ratio, CO-to-H₂ conversion factor and galaxy inclinations where applicable. One finds good qualitative agreement between our data and the measurements from other studies despite a variety of applied star formation rate tracers. This combined data distribution is indicative of 3 distinctly different regimes (indicated by the vertical lines) for the star formation law (see discussion in the text).

cussed in § 6.2, measurements from starburst galaxies (Kennicutt 1998a), and data from low surface brightness galaxies (LSB, Wyder et al., in prep.). Our data and those from the literature sweep out a clear, consistent trend in SFR-gas space. The ‘kink’ in the pixel-by-pixel distribution (indicated by the left vertical line), reflecting the saturation of H I at $\Sigma_{\text{gas}} \approx 9 \text{ M}_{\odot} \text{ pc}^{-2}$ as discussed in § 3.5 and § 4.1, is also visible in the data distribution from the other studies.

In the following we will discuss how the results from this study relate to the work of K98, which is the only study so far to explore the SF law over the full range of Σ_{SFR} and Σ_{gas} shown in Figure 15, and we will discuss

a possible transition that may be expected at around $\Sigma_{\text{gas}} \approx 200 \text{ M}_{\odot} \text{ pc}^{-2}$ (right vertical line in Figure 15).

In this paper, we find $\Sigma_{\text{SFR}} \propto \Sigma_{\text{H}_2}^{1.0 \pm 0.2}$, whereas K98 found a power law with slope $N = 1.40 \pm 0.15$ relating Σ_{SFR} and Σ_{gas} . The fit of K98 depends on the contrast between normal spirals, $\Sigma_{\text{H}_2} \approx 20 \text{ M}_{\odot} \text{ pc}^{-2}$, and high surface density starbursts, $\Sigma_{\text{H}_2} \approx 1000 \text{ M}_{\odot} \text{ pc}^{-2}$. A power law index $N \approx 1.5$ relating SFR to CO emission has been well-established in starbursts at low and high redshifts by a number of authors (e.g., Gao & Solomon 2004; Riechers et al. 2007). There may be reasons to expect different values of N in starburst environments and in our data. Starburst galaxies have average sur-

face densities far in excess of a Galactic GMC (e.g., Gao & Solomon 2004; Rosolowsky & Blitz 2005). We have no such regions in our own sample, instead we make our measurements in the regime where $\Sigma_{\text{H}_2} = 3 - 50 \text{ M}_\odot \text{ pc}^{-2}$. In starbursts, the changes in molecular surface density must reflect real changes in the physical conditions being observed.

In our data, Σ_{H_2} is likely to be a measure of the filling factor of GMCs rather than real variations in surface density. On the one hand, for our resolution (750 pc) and sensitivity ($\Sigma_{\text{H}_2} = 3 \text{ M}_\odot \text{ pc}^{-2}$) the minimum mass we can detect along a line of sight is $\sim 1.5 \cdot 10^6 \text{ M}_\odot$. Most of the mass in Galactic GMCs is in clouds with $M_{\text{H}_2} \approx 5 \cdot 10^5 - 10^6 \text{ M}_\odot$ (e.g., Blitz 1993). Consequently, wherever we detect H_2 we expect at least a few GMCs in our beam. On the other hand, most of our data have $\Sigma_{\text{H}_2} \lesssim 50 \text{ M}_\odot \text{ pc}^{-2}$. The typical surface density of a Galactic GMC is $170 \text{ M}_\odot \text{ pc}^{-2}$ (Solomon et al. 1987). These surface densities are much lower than those observed in starbursts and are consistent with Galactic GMCs filling $\lesssim 1/3$ of the beam. If GMC properties are the same in all spirals in our sample, then for this range of surface densities we expect a power law index of $N = 1$ as Σ_{H_2} just represents the beam filling fraction of GMCs. Averaging over at least a few clouds may wash out cloud-cloud variations in the SFE. A test of this interpretation is to measure GMC properties in a wide sample of spirals. We note that Local Group spirals display similar scaling relations and cloud mass distribution functions so that it is hard to distinguish GMCs in M 31 or M 33 from those in the Milky Way (e.g., Blitz et al. 2007; Bolatto et al. 2008). If this holds for all spirals, then we may indeed expect $N = 1$ whenever GMCs represent the dominant mode of star formation. The next generation of mm-arrays should soon be able to measure GMC properties beyond the Local Group and shed light on this topic. In that sense, our measurement of $N = 1.0 \pm 0.2$ represents a prediction that GMC properties are more or less universal in nearby spiral galaxies.

For our results to be consistent with those from starbursts, the slope must steepen near $\Sigma_{\text{H}_2} \approx 200 \text{ M}_\odot \text{ pc}^{-2}$. This might be expected on both observational and physical grounds. CO is optically thick at the surfaces of molecular clouds. Therefore, as the filling fraction of such clouds for a given telescope beam approaches unity, CO will become an increasingly poor measure of the true Σ_{H_2} because of the optical thickness of the CO emission. Even if such clouds have Galactic SFEs, the observed relationship between CO and an optically thin SFR tracer, e.g., far infrared (FIR) emission, will steepen. It is also likely that physical conditions inside the molecular gas change as surface densities exceed that of a typical GMC (e.g., Padoan et al. 2007). If the density increases, the free fall time within the gas will decrease, possibly leading to more efficient star formation (e.g., Krumholz & McKee 2005). We refer the reader to Krumholz & Thompson (2007) for a full treatment of theoretical expectations for changing Schmidt laws.

In fact, Gao & Solomon (2004) may observe the transition directly; in their Figures 1b and 3 they show that

FIR emission (i.e., the SFR) scales linearly with CO emission below $M_{\text{H}_2} \approx 10^{10} \text{ M}_\odot$, i.e., for their sample of ‘normal’ spiral galaxies. Above 10^{10} M_\odot , i.e., for LIRGs and ULIRGs, they observe a steeper power law index relating SFR to CO (while the relationship between SFR and dense gas, as traced by HCN emission, remains linear). This value, $M_{\text{H}_2} \approx 10^{10} \text{ M}_\odot$, is about the upper limit of molecular gas masses observed in our sample of spiral galaxies (see Table 5 in Leroy et al. 2008a). Based on our results, we suggest that the former (linear) regime corresponds to star formation organized into normal spiral GMCs.

If this sketch is correct, then care must be taken relating the SFR to CO measurements. The efficiency with which gas forms stars will depend on what regime one considers. Perhaps more excitingly, the reverse is also true: by measuring the SFE one can place a region or galaxy in either the ‘starburst’ or ‘GMC/disk’ regime. This offers the intriguing prospect, for example, of diagnosing the dominant mode of star formation in surveys of star formation and molecular gas at high redshift that will be a major component of ALMA science. Even with the current generation of millimeter-wave telescopes such comparisons are possible. For example, Daddi et al. (2008) recently showed that molecular gas in ‘BzK’-selected galaxies at $z = 1.5$ has the same FIR-to-CO ratio (and thus presumably SFE) as local spiral galaxies. For comparison, sub-millimeter (‘SCUBA’) galaxies display dramatically higher SFEs, as traced by their FIR-to-CO ratios (e.g., Greve et al. 2005). A suggestive link to this work is that the BzK galaxies show signs of larger stellar disks and more extended CO emission, completely consistent with star formation proceeding mostly in a disk populated by GMCs analogous to those in nearby galaxies.

The authors thank the teams of SINGS, the GALEX NGS and BIMA SONG for creating and making available their outstanding datasets and the anonymous referee for providing useful comments. Furthermore we would like to thank R. Kennicutt, K. F. Schuster, T. Wong, L. P. Crosthwaite, S. Jogee and their collaborators for making their data available. We are grateful to Rob Kennicutt and Daniela Calzetti for many useful discussions and suggestions. F.B. acknowledges support from the Deutsche Forschungsgemeinschaft (DFG) Priority Program 1177. E.B. gratefully acknowledges financial support through an EU Marie Curie International Reintegration Grant (Contract No. MIRG-CT-6-2005-013556). The work of W.J.G.d.B. is based upon research supported by the South African Research Chairs Initiative of the Department of Science and Technology and National Research Foundation. We have made use of the Extragalactic Database (NED), which is operated by the Jet Propulsion Laboratory, California Institute of Technology, under contract with the National Aeronautics and Space Administration. This research has made use of NASA’s Astrophysics Data System (ADS).

REFERENCES

Blitz, L. 1993, *Protostars and Planets III*, 125

Blitz, L., Fukui, Y., Kawamura, A., Leroy, A., Mizuno, N. & Rosolowsky, E. 2007, *Protostars and Planets V*, 81

- Boissier, S. & Prantzos, N. 1999, *MNRAS*, 307, 857
 Boissier, S., Prantzos, N., Boselli, A. & Gavazzi, G. 2003, *MNRAS*, 346, 1215
 Bolatto, A. D., et al. 2008, *ApJ*, accepted, astro-ph/0807.0009
 Boselli, A., Gavazzi, G., Lequeux, J., Buat, V., Casoli, F., Dickey, J. & Donas, J. 1995, *A&A*, 300, L13
 Braine, J., Combes, F., Casoli, F., Dupraz, C., Gerin, M., Klein, U., Wielebinski, R. & Brouillet, N. 1993, *A&AS*, 97, 887
 Buat, V., Deharveng, J. M. & Donas, J. 1989, *A&A*, 223, 42
 Buat, V. 1992, *A&A*, 264, 444
 Calzetti, D., et al. 2005, *ApJ*, 633, 871
 Calzetti, D., et al. 2007, *ApJ*, 666, 870
 Crosthwaite, L. P., & Turner, J. L. 2007, *AJ*, 134, 1827
 Daddi, E., Dannerbauer, H., Elbaz, D., Dickinson, M., Morrison, G., Stern, D. & Ravindranath, S. 2008, *ApJ*, 673, L21
 Dame, T. M., Hartmann, D. & Thaddeus, P. 2001, *ApJ*, 547, 792
 Deharveng, J.-M., Sasseen, T. P., Buat, V., Bowyer, S., Lampton, M. & Wu, X. 1994, *A&A*, 289, 715
 de Vaucouleurs, G., et al. 1991, Springer, Volume 1-3, XII, 2069
 Federman, S. R., Glassgold, A. E. & Kwan, J. 1979, *ApJ*, 227, 466
 Gao, Y. & Solomon, P. M. 2004, *ApJ*, 606, 271
 Gil de Paz, A., et al. 2007, *ApJS*, 173, 185
 Gordon, K. D., et al. 2005, *PASP*, 177, 503
 Greve, T. R., et al. 2005, *MNRAS*, 359, 1165
 Hamajima, K. & Tosa, M. 1975, *PASJ*, 27, 561
 Hartwick, F. D. A. 1971, *ApJ*, 163, 431
 Helfer, T. T., Thornley, M. D., Regan, M. W., Wong, T., Sheth, K., Vogel, S. N., Blitz, L. & Bock, D. C.-J. 2003, *ApJS*, 145, 259
 Heyer, M. H., Corbelli, E., Schneider, S. E. & Young, J. S. 2004, *ApJ*, 602, 723
 Hunter, D. A., Elmegreen, B. G. & Baker, A. L. 1998, *ApJ*, 493, 595
 Isobe, T., Feigelson, E. D., Akritas, M. G. & Babu, G. J. 1990, *ApJ*, 364, 104
 Israel, F. P. 1997, *A&A*, 328, 471
 Jogee, S., Scoville, N., & Kenney, J. D. P. 2005, *ApJ*, 630, 837
 Jörsäter, S. & van Moorsel, G. A. 1995, *AJ*, 110, 2037
 Karachentsev, I. D., et al. 2002, *A&A*, 383, 125
 Karachentsev, I. D., et al. 2003, *A&A*, 398, 479
 Kennicutt, R. C. 1989, *ApJ*, 344, 685
 Kennicutt, R. C. 1998a, *ApJ*, 498, 541
 Kennicutt, R. C., 1998b, *ARA&A*, 36, 189
 Kennicutt, R. C., Jr., et al. 2003, *PASP*, 115, 928
 Kennicutt, R. C., Jr., et al. 2007, *ApJ*, 671, 333
 Kroupa, P., 2001, *MNRAS*, 322, 231
 Krumholz, M. R. & McKee, C. F. 2005, *ApJ*, 630, 250
 Krumholz, M. R. & Thompson, T. A. 2007, *ApJ*, 669, 289
 Kuno, N., et al. 2007, *PASJ*, 59, 117
 Lee, J. C., 2006, PhD Thesis, University of Arizona
 Leitherer, C., et al. 1999, *ApJS*, 123, 3
 Leroy, A., Bolatto, A. D., Simon, J. D. & Blitz, L. 2005, *ApJ*, 625, 763
 Leroy, A., Bolatto, A., Stanimirovic, S., Mizuno, N., Israel, F., & Bot, C. 2007, *ApJ*, 658, 1027
 Leroy, A., et al. 2008a, *AJ*, accepted
 Leroy, A., et al. 2008b, *AJ*, submitted
 Madden, S. C., Poglitsch, A., Geis, N., Stacey, G. J., & Townes, C. H. 1997, *ApJ*, 483, 200
 Madore, B. F., van den Bergh, S. & Rogstad, D. H. 1974, *ApJ*, 191, 317
 Madore, B. F. 1977, *MNRAS*, 178, 1
 Martin, C. L. & Kennicutt, R. C. 2001, *ApJ*, 555, 301
 Matteucci, F., Panagia, N., Pipino, A., Mannucci, F., Recchi, S. & Della Valle, M. 2006, *MNRAS*, 372, 265
 Misiriotis, A., Xilouris, E. M., Papamastorakis, J., Boumis, P. & Goudis, C. D. 2006, *A&A*, 459, 113
 Morris, M., & Lo, K. Y. 1978, *ApJ*, 223, 803
 Morrissey, P., et al. 2005, *ApJ*, 619, L7
 Moustakas, J., et al. 2006, *ApJ*, 651, 155
 Newton, K. 1980, *MNRAS*, 190, 689
 Padoan, P., Nordlund, Å., Kritsuk, A. G., Norman, M. L., & Li, P. S. 2007, *ApJ*, 661, 972
 Pérez-González, P. G., et al. 2006, *ApJ*, 648, 987
 Prugniel, P. & Heraudeau, P. 1998, *A&AS*, 128, 299
 Riechers, D. A., Walter, F., Carilli, C. L. & Bertoldi, F. 2007, *ApJ*, 671, L13
 Rieke, G., et al. 2004, *ApJS*, 154, 25
 Rosolowsky, E. & Blitz, L. 2005, *ApJ*, 623, 826
 Salim, S., et al. 2007, *ApJS*, 173, 267
 Salpeter, E. E., 1955, *ApJ*, 121, 161
 Sanduleak, N. 1969, *AJ*, 74, 47
 Schaye, J. 2004, *ApJ*, 609, 667
 Schlegel, D. J., Finkbeiner, D. P. & Davis, M. 1998, *ApJ*, 500, 525
 Schmidt, M. 1959, *ApJ*, 129, 243
 Schuster, K. F., et al. 2004, *A&A*, 423, 1171
 Schuster, K. F., Kramer, C., Hitschfeld, M., Garcia-Burillo, S. & Mookerjee, B. 2007, *A&A*, 461, 143
 Skaya, E. J. & Federman, S. R. 1987, *ApJ*, 319, 76
 Solomon, P. M., Rivolo, A. R., Barrett, J. & Yahil, A. 1987, *ApJ*, 319, 730
 Spoon, H. W. W. 2003, Ph.D. Thesis
 Springel, V. & Hernquist, L. 2003, *MNRAS*, 339, 289
 Strong, A. W. & Mattox, J. R. 1996, *A&A*, 308, L21
 Tamburro, D., et al. 2008, *AJ*, accepted
 Tan, J. C., Silk, J. & Balland, C. 1999, *ApJ*, 522, 579
 Taylor, C. L., Kobulnicky, H. A. & Skillman, E. D. 1998, *AJ*, 116, 2746
 Thilker, D. A., et al. 2005, *ApJ*, 619, L79
 Thornley, M. D. & Wilson, C. D. 1995, *ApJ*, 447, 616
 Tosa, M. & Hamajima, K. 1975, *PASJ*, 27, 501
 Walter, F. & Brinks, E. 1999, *AJ*, 118, 273
 Walter, F., Taylor, C. L., Hüttemeister, S., Scoville, N. & McIntyre, V. 2001, *AJ*, 121, 727
 Walter, F. 2008, *AJ*, accepted
 Wilson, C. D. 1995, *ApJ*, 448, L97
 Wong, T. & Blitz, L. 2002, *ApJ*, 569, 157
 Wyder, T., et al. 2007, *ApJS*, 173, 293
 Young, J. S., et al. 1995, *ApJS*, 98, 219